

Towards High-Field MRI Systems: Design Strategy for the TEM Resonator

Nadine Kolment

Master's of Electrical Engineering

Department of Electrical Engineering

McGill University

Montreal, Quebec

December 2013

A thesis submitted to McGill University in partial fulfilment of the requirements of
the degree of Master's in Electrical Engineering

©Nadine Kolment 2013

ACKNOWLEDGEMENTS

Many contributed to this research project and I am immensely indebted to them for helping me reach my objectives. First and foremost, I would like to thank my supervisor Dr Milica Popovich for her unwavering support and her profound enthusiasm towards academic research and all things of life that forges a balanced scientist. I am also very grateful to Dr Bruce Pike and Dr Simone A. Winkler, whose recommendations were pivotal in the early stages of the project. My thanks go to all the members of the Computational Electromagnetics Laboratory of McGill University, particularly to the doctoral candidates Evgeny Kirshin, Emily Porter and Adam Santorelli, for their constant encouragement and constructive criticism throughout the project. Finally, I would like to thank my family and friends for their love and support.

ABSTRACT

High-field magnetic resonance imaging (MRI) is a very promising concept as it benefits from a significant improvement in the signal-to-noise ratio (SNR), a measure that directly affects image resolution. However, as the resonant wavelength approaches the dimensions of the object being imaged, the wave propagation effects of the radio frequency (RF) field significantly deteriorate the uniformity of the excitation pattern, thus leading to contrast aberrations and distortions in the resulting image. Recent proof-of-concept studies have shown the merits of parallel transmission techniques in accurately controlling the RF magnetic field whereas novel coil arrangements, such as the TEM resonator, have provided the necessary platform for conducting truly parallel excitations experiments. The purpose of this thesis is to provide a comprehensive study on the design of the TEM resonator by comparing two modelling techniques. The first technique uses multi-conductor transmission line theory to model the coil; the second technique uses the brute-force computational algorithm called finite-difference time-domain (FDTD). The two techniques are compared in terms of the S_{11} trends observed while varying TEM resonator design parameters such as the capacitor values and the line element geometry. A difference of 15% in the coil response was observed for an MRI system of 3-Tesla field strength. This modelling error increases with resonant frequency and reaches the 40% mark for a high-field MRI system of 7-Tesla field strength. Despite the diverging results for increasing frequency, this study shows that the variation of design parameters in each modelling technique exhibit comparable trends.

ABRÉGÉ

L'imagerie par résonance magnétique (IRM) à haut champ est un concept très promettant car elle bénéficie d'une amélioration importante du rapport signal-bruit, une mesure qui affecte directement la résolution de l'image. Cependant, quand la longueur d'onde de résonance se rapproche des dimensions de l'objet sous examination, les effets de propagation d'onde du champ radiofréquence (RF) détériore de façon significative l'uniformité du motif de champ d'excitation, ainsi menant à des aberrations de contraste et des distortions dans l'image. Des études récentes ont validé le principe de transmission parallèle pour contrôler le champ magnétique RF tandis que de nouveaux arrangements d'antennes, tel que le résonateur TEM, ont permis des expériences avec des transmission réellement en parallèle. Le but de ce mémoire est d'étudier la conception du résonateur TEM en comparant deux techniques de modélisation. La première technique utilise la théorie de ligne de transmission à conducteurs multiples; la deuxième technique utilise un algorithme de calcul par force brute: la méthode des différences finies dans le domaine temporel (FDTD). Les deux techniques sont comparées par rapport aux tendances observées lorsque les paramètres du résonateur TEM, tel que la valeur des condensateurs et la géométrie des lignes microbandes, sont variés. Une différence de 15% dans la réponse de l'antenne a été observé pour un système d'IRM de 3 Tesla. L'erreur de modélisation augmente avec la fréquence de résonance pour atteindre 40% dans un système d'IRM de 7 Tesla. Malgré les résultats divergents, cette étude démontre que

la variation des paramètres de l'antenne présente des tendances comparables dans les deux méthodes.

TABLE OF CONTENTS

| | |
|--|------|
| ACKNOWLEDGEMENTS | ii |
| ABSTRACT | iii |
| ABRÉGÉ | iv |
| LIST OF TABLES | viii |
| LIST OF FIGURES | ix |
| List of Abbreviation | xii |
| List of Symbols | xiii |
| 1 Introduction | 1 |
| 2 Background | 4 |
| 2.1 Magnetic Resonance Imaging | 4 |
| 2.2 Electromagnetic Fields Due to Magnetic Moments | 7 |
| 2.3 Selective Excitation | 10 |
| 2.4 Parallel Transmission | 13 |
| 3 Transmit Coil Simulation Models | 19 |
| 3.1 The TEM Resonator | 19 |
| 3.2 MTL Model | 23 |
| 3.2.1 MTL Equations | 24 |
| 3.2.2 Poisson's Equations | 27 |
| 3.2.3 Per Unit Length Parameters | 31 |
| 3.2.4 Model Measurements | 39 |
| 3.3 Three-Dimensional Full-Wave EM Model | 47 |
| 3.3.1 FDTD Method | 48 |

| | | |
|-------|---|----|
| 4 | Transmit Coil Model Measurements | 52 |
| 4.1 | MTL Model Results | 52 |
| 4.1.1 | Coil Parameter Characterization | 53 |
| 4.1.2 | Coil Parameter Selection | 56 |
| 4.2 | Full-Wave EM Model Results | 60 |
| 4.2.1 | Coil Parameter Characterization | 60 |
| 4.2.2 | Comparison of the MTL Model and the Full-Wave Model . | 63 |
| 4.2.3 | Coil Parameter Selection | 66 |
| 4.3 | Loaded Coil Adjustments | 69 |
| 5 | Conclusion | 72 |
| 5.1 | Summary | 72 |
| 5.2 | Future Work | 73 |
| A | Transmission Line Theory | 75 |
| A.1 | Current Equation | 76 |
| A.2 | Voltage Equation | 82 |
| | References | 88 |

LIST OF TABLES

| <u>Table</u> | | <u>page</u> |
|--------------|--|-------------|
| 4-1 | The TEM resonator parameter settings determined by the MTL model for the 3T (128 MHz) and 7T (300 MHz) coils. | 58 |
| 4-2 | The TEM resonator parameter settings determined by the full-wave model for the 3T (128 MHz) and 7T (300 MHz) coils. | 67 |
| 4-3 | The electromagnetic properties of the human head phantom as calculated by [1]. | 69 |
| 4-4 | The TEM resonator parameter settings determined by the full-wave EM model for the 3T (128 MHz) and 7T (300 MHz) coils, adjusted for the loading effects. | 70 |

LIST OF FIGURES

| <u>Figure</u> | | <u>page</u> |
|---------------|--|-------------|
| 2-1 | Magnetic field components due to $m_x(t)$ and $m_y(t)$ | 9 |
| 3-1 | The TEM resonator: (a) the model of the an 8-element coil with the end-capacitors and sources, (b) the current flow diagram and (c) the single-element building block of the TEM resonator. | 21 |
| 3-2 | The cross-sectional schematic of the TEM resonator. | 22 |
| 3-3 | The electric field resulting from conduction losses along the length of two parallel waveguides. | 24 |
| 3-4 | The cross-section of the TEM resonator annotated with the path c around the i -th conductor; the path c' from conductor j to i ; and the Poisson boundary conditions prescribed in Equation 3.26 | 33 |
| 3-5 | A 16-port network representation of the line elements and shield. . . . | 41 |
| 3-6 | The TEM resonator network connected to the load-side capacitors Z_{iL} , for $i = 1\dots 8$ | 42 |
| 3-7 | The full circuit representation of the TEM resonator driven by a source V_S on the first conductor. The red arrows indicate the direction of the currents used in the mesh analysis. | 44 |
| 3-8 | The Yee cell (adapted from [2]). | 51 |
| 4-1 | The S_{11} spectrum of the TEM resonator predicted by the MTL model, where the capacitor values are set to 10 pF and the width and thickness of the line elements are 24 mm and 35 μm , respectively. | 53 |
| 4-2 | The comparison of the S_{11} spectra from the MTL model for varying line element thicknesses. These curves show an upward shift in the resonance for increasing line element thickness. | 54 |

| | | |
|------|---|----|
| 4-3 | The comparison of the S_{11} spectra from the MTL model for varying line element widths. These curves show a downward shift in the resonance for increasing line element width. | 55 |
| 4-4 | The comparison of the S_{11} spectra from the MTL model for varying capacitor values. These curves show an downward shift in the resonance for increasing capacitor values. | 56 |
| 4-5 | The S_{11} spectra of the 3T (128 MHz) and 7T (300 MHz) TEM resonator predicted by the MTL model. | 58 |
| 4-6 | The normalized (a) electric and (b) magnetic field magnitude distribution of the 3T (128 MHz) TEM resonator predicted by the MTL model, at the $z = L/2$ cross-section. The two inner circles drawn in black delimit the dielectric subdomain, whereas the intersections of the straight lines and the most inner circle mark the edges of the line elements. | 59 |
| 4-7 | The normalized (a) electric and (b) magnetic field magnitude distribution of the 7T (300 MHz) TEM resonator predicted by the MTL model, at the $z = L/2$ cross-section. The two inner circles drawn in black delimit the dielectric subdomain, whereas the intersections of the straight lines and the most inner circle mark the edges of the line elements. | 59 |
| 4-8 | The S_{11} spectrum of the TEM resonator predicted by the full-wave EM model, where the capacitor values are set to 10 pF and the width and thickness of the line elements are 24 mm and 35 μm , respectively. | 60 |
| 4-9 | The comparison of the S_{11} spectra from the full-wave EM model for varying line element thicknesses. These curves show an upward shift in the resonance for increasing line element thickness. | 61 |
| 4-10 | The comparison of the S_{11} spectra from the full-wave EM model for varying line element widths. These curves show an upward shift in the resonance for increasing line element widths. | 62 |
| 4-11 | The comparison of the S_{11} spectra from the full-wave EM model for varying capacitor values. These curves show a downward shift in the resonance for increasing capacitor values. | 63 |

| | | |
|------|---|----|
| 4-12 | The comparison of the (a) resonance frequency, f_0 , and (b) the S_{11} parameter (in dB) calculated by the MTL model and full-wave EM model for varying line element widths. | 64 |
| 4-13 | The comparison of the (a) resonance frequency, f_0 , and (b) the S_{11} parameter (in dB) calculated by the MTL model and full-wave EM model for varying capacitor values. | 65 |
| 4-14 | The S_{11} spectra of the 3T (128 MHz) and 7T (300 MHz) resonator predicted by the full-wave EM model. | 67 |
| 4-15 | The normalized (a) electric and (b) magnetic field magnitude distribution of the 3T (128 MHz) TEM resonator predicted by the full-wave model, at the $z = L/2$ cross-section. | 68 |
| 4-16 | The normalized (a) electric and (b) magnetic field magnitude distribution of the 7T (300 MHz) TEM resonator predicted by the full-wave model, at the $z = L/2$ cross-section. | 68 |
| 4-17 | The comparison of the S_{11} spectra of the unloaded (blue); loaded (black); and loaded and adjusted (read) TEM resonators predicted by the full-wave EM model. | 70 |
| 4-18 | The normalized (a) electric and (b) magnetic field magnitude distribution of the loaded and adjusted 3T (128 MHz) TEM resonator predicted by the full-wave model, at the $z = L/2$ cross-section. . . . | 71 |
| 4-19 | The normalized (a) electric and (b) magnetic field magnitude distribution of the loaded and adjusted 7T (300 MHz) TEM resonator predicted by the full-wave model, at the $z = L/2$ cross-section. . . . | 71 |
| A-1 | A multi-conductor transmission line of N conductors where a cylindrical surface S of length Δz was placed around one of the conductors. | 78 |
| A-2 | A multi-conductor transmission line of N conductors where an open surface S of length Δz was placed between one conductor and the reference conductor. | 83 |

List of Abbreviation

EM: electromagnetic
FD: finite difference
FDTD: finite-difference time-domain
FEM: finite-element method
FOR: frame of reference
FOX: field of excitation
MoM: method of moments
MR: magnetic resonance
MRI: magnetic resonance imaging
MTL: multi-conductor transmission line
NMR: nuclear magnetic resonance
PDE: partial differential equation
PUL: per-unit-length
RF: radio frequency
SENSE: sensitivity encoding
SNR: signal-to-noise ratio
TEM: transverse electromagnetic

List of Symbols

B_0 : main static magnetic field, in teslas (T)

B_1^+ : RF excitation magnetic field, in teslas (T)

γ : gyromagnetic ratio, in radians per second per tesla (rad/s/T)

$\vec{k}(t)$: k -space trajectory, in per meter (1/m)

\vec{m} : magnetization vector, in amperes per meter (A/m)

\vec{m}_z : longitudinal magnetization vector, in amperes per meter (A/m)

\vec{m}_{xy} : transverse magnetization vector, in amperes per meter (A/m)

\vec{m}_r : transverse magnetization vector in rotating FOR, in amperes per meter (A/m)

∇ : Scalar Laplacian operator

T_1 : spin-lattice time constant, in seconds (s)

T_2 : spin-spin time constant, in seconds (s)

CHAPTER 1

Introduction

Magnetic resonance imaging (MRI) is a powerful medical imaging technique that allows for visualization of internal structures of the body in a completely non-invasive manner. It has evolved immensely since its inception in 1952, making it one of the most useful tools in medicine today. Many important discoveries over the last two decades have broadened the range of applications, from basic musculoskeletal imaging to functional MRI and brain imaging. Through recent advances in magnet fabrication, MRI systems are becoming increasingly precise and powerful. When subject to a stronger static magnetic field, the signal-to-noise ratio (SNR) of the radio frequency (RF) coils improves drastically, resulting in greater image quality [3]. However, the increase in magnetic field strength poses many technical challenges. According to Larmor's equation, the natural resonant frequency, ω_0 (in rads per second), — and thus, the RF coil operating frequency — increases proportionally with respect to the strength of the main magnetic field B_0 (in teslas). In today's standard clinical systems, where B_0 is at most 3 T, the wavelength of the RF excitation magnetic field propagating in the tissue, commonly referred to as the B_1^+ -field (in teslas), is large relative to the object being imaged. In these conditions, the phase-related effects that arise in the tissues are very small and have a negligible effect on the uniformity of the B_1^+ -field. However, as the operating frequency increases with field strengths greater than 4 T, the uniformity of the RF field quickly deteriorates [4].

Many solutions have been proposed to compensate for the B_1^+ pattern deviations. The travelling wave scheme consists of RF waves radiating from an antenna and propagating into a cylindrical waveguide which contains the subject [5]. This approach has proven to generate a very homogeneous field, due to the minor presence of standing waves and the absence of coupling between the antenna and the patient. However, it is not possible to spatially limit the field of excitation (FOX) to anything other than the volume of the actual waveguide, which can have a big impact on managing the noise contribution to the magnetic resonance (MR) signal [6]. Other solutions rely on more traditional MRI hardware which allows for spatially-selective excitation. With the use of multi-element parallel transmission coils and time-varying gradients, novel RF pulse designs are revamping well-established B_1^+ correction techniques, such as static B_1^+ shimming and transmit sensitivity encoding (transmit SENSE), to improve homogeneity and reduce the risk of RF-induced tissue heating.

The TEM resonator is an MRI RF coil which has gained a lot of attention over the last decade. It had been shown to maintain better magnetic field homogeneity and operate more efficiently than the traditional volume coils at frequencies above 200 MHz [7]. More recently, the multi-channel capabilities of the TEM resonator have enabled truly parallel RF pulse transmission experiments. Given the importance of this coil, many studies focus on developing models and tools to facilitate its design and verification. Although full-wave modelling is an essential and necessary step for the design of any high-field MRI coil [8], simplified models have been developed to accelerate the design time. The focus of this study is to investigate on a

strategy for designing TEM resonators in the context of high-field MRI applications. Two prominent coil models — the multi-conductor transmission line and the FDTD method — are compared in terms of their performance in both the standard and high-field MRI frequency range.

The present document is separated into five chapters. Following this introduction, a review of the relevant literature is given in order to familiarize the reader with the important concepts of MRI. A description of the methods used to conduct the experiment is laid out in Chapter 3. The results and the discussion are presented in Chapter 4. Finally, a summary of the study is given in the concluding chapter.

CHAPTER 2 Background

2.1 Magnetic Resonance Imaging

Magnetic resonance imaging relies on a phenomenon called nuclear magnetic resonance (NMR). Atomic nuclei (i.e. protons and neutrons) have an intrinsic angular momentum called "spin". Since protons are charged particles, the spinning motion creates a magnetic moment. The proton's angular momentum \vec{L} (in kilogram-meters-square per second) and magnetic moment $\vec{\mu}$ (in ampere-square meters) are related by a special quantity, called the gyromagnetic ratio γ (in radians per second per tesla):

$$\vec{\mu} = \gamma \vec{L} \tag{2.1}$$

Although neutrons do not exhibit a charge, there is an overall magnetic moment due to the neutron's sub-composition of electrically charged particles. The overall nuclear spin and magnetic moment of an atom, and thus the overall observable gyromagnetic ratio, depend on the number of protons and neutrons that constitute the nuclide. In the case of hydrogen 1H , the nuclide species of interest in MRI, the gyromagnetic ratio is 267.53 rad/s/T — or equivalently, 42.58 MHz/T.

In the absence of a magnetic field, the individual nuclear magnetic moments align randomly, producing an overall zero magnetization at equilibrium. In the presence of a magnetic field, the individual magnetic moments align either parallel or anti-parallel to the field. The parallel alignment is a lower-energy state compared to the

anti-parallel alignment and is slightly preferred. Macroscopically, the small bias in favour of the parallel alignment creates a net magnetization vector that points in the same direction as the applied field.

Under a static magnetic field, the magnetic moment $\vec{\mu}$ experiences a torque \vec{T} (in newton-meters):

$$\vec{T} = \vec{\mu} \times \vec{B} \quad (2.2)$$

By definition, torque is the time rate of change of angular momentum:

$$\vec{T} = \frac{d\vec{L}}{dt} \quad (2.3)$$

Hence, the time rate of change of $\vec{\mu}$ is related to the torque:

$$\gamma\vec{T} = \frac{d\gamma\vec{L}}{dt} = \frac{d\vec{\mu}}{dt} = \gamma\vec{\mu} \times \vec{B} \quad (2.4)$$

By summing over a unit volume, equation 2.4 is expressed in terms of the magnetization vector \vec{m} (in amperes per meter):

$$\frac{d\vec{m}}{dt} = \gamma\vec{m} \times \vec{B} \quad (2.5)$$

As per MRI convention, the main static magnetic field is denoted as \vec{B}_0 and its direction is assigned to the z -axis. Equation 2.5 can be separated component-wise and solved for each component as follows:

$$m_x = m_{x0} \cos(\gamma B_0 t) - m_{y0} \sin(\gamma B_0 t) \quad (2.6a)$$

$$m_y = m_{y0} \cos(\gamma B_0 t) + m_{x0} \sin(\gamma B_0 t) \quad (2.6b)$$

$$m_z = m_{z0} \quad (2.6c)$$

where the vector $[m_{x0}, m_{y0}, m_{z0}]$ is the initial condition of \vec{m} and B_0 is the magnitude of the applied main magnetic field. These equations describe a precessional motion of the net magnetization vector \vec{m} about the z -axis. The angular frequency of this motion is called the Larmor frequency and is directly related to the gyromagnetic ratio:

$$\omega_0 = \gamma B_0 \quad (2.7)$$

In today's clinical MRI systems, the main magnetic field B_0 ranges from 0.5 to 3T, which implies resonant frequencies ranging from 21.3 to 128 MHz.

Concurrently with the precessional motion, the magnetic moments progressively realign themselves to the B_0 -field to reach thermal equilibrium. This relaxation can be thought of as two processes: the decay of the transverse magnetization m_{xy} , the magnetization components perpendicular to the B_0 -field; and the regrowth of the longitudinal magnetization m_z to equilibrium state. The longitudinal magnetization relaxation is attributed to spin-lattice interactions. The nuclei exchange energy with their surrounding lattice when transitioning to a lower energy state (ie. parallel alignment). m_z approaches its equilibrium state exponentially with time constant T_1 :

$$m_z(t) = M_o + (m_{z0} - M_o)e^{-t/T_1} \quad (2.8)$$

The transverse magnetization m_{xy} relaxation is attributed to spin-spin interactions. Polarization in the transverse plane disappears more quickly than its re-appearance in the longitudinal direction due to loss of phase coherence between the individual

dipoles. m_{xy} approaches its equilibrium state exponentially with time constant T_2 :

$$m_{xy}(t) = M_o e^{-t/T_2} \quad (2.9)$$

Combining the nuclear mechanisms of precession and relaxation, the overall behaviour of the net magnetization vector is described by the Bloch equation:

$$\frac{d\vec{m}}{dt} = \gamma \vec{m} \times \vec{B} - \frac{m_x \hat{i} + m_y \hat{j}}{T_2} - \frac{(m_z - M_o) \hat{k}}{T_1} \quad (2.10)$$

2.2 Electromagnetic Fields Due to Magnetic Moments

Ignoring the effects of relaxation, the individual nuclear magnetic moments can be approximated as very small magnetic dipoles. The complete electromagnetic (EM) field expression (valid in near- as well as far-field regions) for an ideal magnetic dipole is:

$$\begin{aligned} E_r &= 0 \\ E_\theta &= 0 \\ E_\phi &= -\frac{I_m l}{4\pi} j\beta \left(1 + \frac{1}{j\beta r}\right) \frac{e^{-j\beta r}}{r} \sin(\theta) \end{aligned} \quad (2.11)$$

$$\begin{aligned} H_r &= \frac{I_m l}{2\pi} j\omega \epsilon \left(\frac{1}{j\beta r} + \frac{1}{(j\beta r)^2}\right) \frac{e^{-j\beta r}}{r} \cos(\theta) \\ H_\theta &= \frac{I_m l}{4\pi} j\omega \epsilon \left(1 + \frac{1}{j\beta r} + \frac{1}{(j\beta r)^2}\right) \frac{e^{-j\beta r}}{r} \sin(\theta) \\ H_\phi &= 0 \end{aligned}$$

where I_m (in amperes) is the hypothetical magnetic current; l (in meters) is the length of the dipole; β is the phase constant and equals $\omega\sqrt{\varepsilon\mu}$; and ε and μ are the electric permittivity (in farads per meter) and the magnetic permeability (in henries per meter), respectively [9].

By definition, the magnetic moment m is equal to $I_m l$. The magnetic field that results from the x-component of the excited (ie. precessing) magnetization vector in equation 2.6c can be found by replacing $I_m l$ in the H-field expressions from equation 2.12 with m_x [10]:

$$\begin{aligned}
 H_{rx} &= \frac{m_x(t)}{2\pi} j\omega\varepsilon \left(\frac{1}{j\beta r} + \frac{1}{(j\beta r)^2} \right) \frac{e^{-j\beta r}}{r} \cos(\theta) \\
 &= F_R(r) m_x(t) \cos(\theta) \\
 H_{\theta x} &= \frac{m_x(t)}{4\pi} j\omega\varepsilon \left(1 + \frac{1}{j\beta r} + \frac{1}{(j\beta r)^2} \right) \frac{e^{-j\beta r}}{r} \sin(\theta) \\
 &= F_R(r) m_x(t) \sin(\theta)
 \end{aligned} \tag{2.12}$$

Similarly, the m_y contribution to the H-field expressions is:

$$\begin{aligned}
 H_{ry} &= \frac{m_y(t)}{2\pi} j\omega\varepsilon \left(\frac{1}{j\beta r} + \frac{1}{(j\beta r)^2} \right) \frac{e^{-j\beta r}}{r} \cos(\theta - 90^\circ) \\
 &= F_R(r) m_y(t) \sin(\theta) \\
 H_{\theta y} &= \frac{m_y(t)}{4\pi} j\omega\varepsilon \left(1 + \frac{1}{j\beta r} + \frac{1}{(j\beta r)^2} \right) \frac{e^{-j\beta r}}{r} \sin(\theta - 90^\circ) \\
 &= -F_R(r) m_y(t) \cos(\theta)
 \end{aligned} \tag{2.13}$$

At a given point of observation $P(r, \theta)$ as shown in Figure 2-1, the radial magnetic fields from the x- and y-component oscillate with a frequency of ω_0 . If a coil is

placed around point P and strategically oriented such that it is normal to the radial field, the precessing magnetization will cause a change of flux Φ (in webers) in the coil and induce a small electromotive force (EMF) $\epsilon = -\frac{d\Phi}{dt}$ (in volts). This signal is commonly called the free induction decay (FID) and it is the MR signal that is picked up by the receiver coil when a sample is excited and resonating at the Larmor frequency.

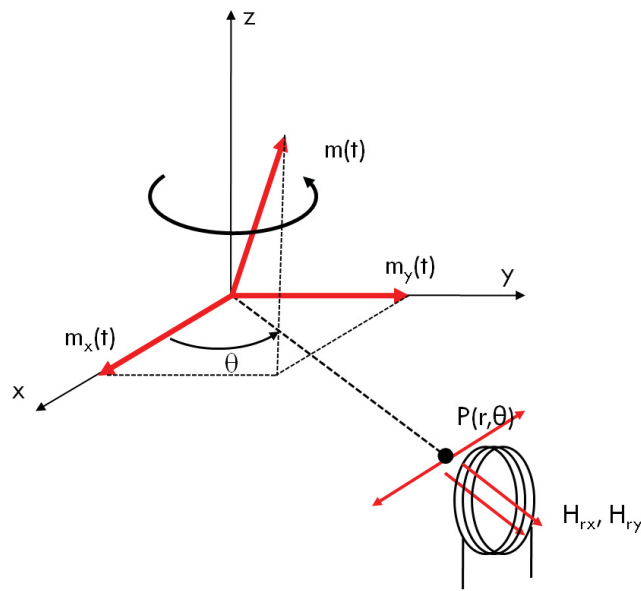


Figure 2-1: Magnetic field components due to $m_x(t)$ and $m_y(t)$.

Analogous to the above description of an excited sample, a sample at equilibrium can be excited into a higher-energy state by absorbing photons at the Larmor frequency. A transmitter coil applying a circularly-polarized magnetic field in the transverse plane rotating at ω_0 will cause a torque on the aligned magnetic moments. Provided that enough energy was absorbed to steer the magnetization vector some

angle away from equilibrium, the magnetization will start precessing about the z-axis and relax back to equilibrium once the B_1^+ -field is turned off.

2.3 Selective Excitation

The transverse magnetization is conventionally expressed as a complex representation of the x - and y -component:

$$m_{xy}(\vec{x}) = m_x(\vec{x}) + jm_y(\vec{x}) \quad (2.14)$$

In the rotating frame of reference (FOR) with angular frequency ω_0 , the transverse component is:

$$m_r(\vec{x}) = m_{x'}(\vec{x}) + jm_{y'}(\vec{x}) \quad (2.15)$$

where x' and y' are rotating axes.

In the small tip-angle regime [11], the transverse magnetization in the rotating FOR after a $B_1^+(t)$ pulse of time T is approximated as:

$$m_r(\vec{x}) = jM_0 \int_0^T \gamma B_1^+(t) e^{j\vec{k}(t)\cdot\vec{x}} dt \quad (2.16)$$

where \vec{x} is the spatial coordinate vector, M_0 is the longitudinal magnetization at thermal equilibrium, γ is the gyromagnetic ratio of the excited nuclei species and $\vec{k}(t)$ is the trajectory traced out in the spatial frequency domain, commonly called k -space, by $\vec{G}(t)$:

$$\vec{k}(t) = -\gamma \int_t^T \vec{G}(\tau) d\tau \quad (2.17)$$

The quantity $\vec{G}(t)$ corresponds to the time-varying gradient magnetic fields. These fields are used to provide spacial localization during the excitation stage and the imaging stage.

Using the sifting property of the three-dimensional delta function ${}^3\delta(\vec{k})$, where $\int_{k_v} f(\vec{k})\delta(\vec{k} - \vec{k}')d\vec{k} = f(\vec{k}')$, (2.16) may be rewritten:

$$m_r(\vec{x}) = jM_0 \int_0^T \gamma B_1^+(t) \int_{k_v} {}^3\delta(\vec{k} - \vec{k}(t)) e^{j\vec{k}\cdot\vec{x}} d\vec{k} dt \quad (2.18)$$

where the k -space integral is defined over the entire FOX k_v [12]. By changing the order of integration and noting that $\delta(\vec{k} - \vec{k}(t)) = \delta(\vec{k}(t) - \vec{k})$ since $\delta(x)$ is an even function,

$$m_r(\vec{x}) = j\gamma M_0 \int_{k_v} \left\{ \int_0^T B_1^+(t) {}^3\delta(\vec{k}(t) - \vec{k}) dt \right\} e^{j\vec{k}\cdot\vec{x}} d\vec{k} \quad (2.19)$$

The inner integral describes a function of \vec{k} that is equal to zero everywhere except on the $\vec{k}(t)$ trajectory. Graphically, it describes a three-dimensional path defined over $\vec{k}(t)$ and weighted explicitly by the RF excitation $B_1^+(t)$. There is also an implicit weighting due to the non-unit, varying speed of $\vec{k}(t)$. Recall the fundamental property of the delta function:

$$\int_{-\infty}^{\infty} \delta(t - a) dt = 1 \quad (2.20)$$

making the term $\delta(t - a)$ have a *unit* weight. Depending on the definition of $\vec{k}(t)$, the expression $\int_{-\infty}^{\infty} {}^3\delta(\vec{k}(t) - \vec{k}) dt$ does not necessarily evaluate to 1. One delta function identity states that:

$$\delta[g(t)] = \sum_i \frac{\delta(t - t_i)}{|g'(t_i)|} \quad (2.21)$$

where t_i are the roots of the expression $g(t)$. The integral of the delta function expression in (2.19) is rewritten to find the non-unit weighting factor by using the

identity in (2.21). Note that the delta function in (2.19) has only one root, $\vec{k}(t) = \vec{k}$.

$$\int_0^T {}^3\delta(\vec{k}(t) - \vec{k})dt = \frac{1}{|\vec{k}'(\vec{k})|} \int_0^T {}^3\delta(t - \vec{k})dt \quad (2.22)$$

The delta function term on the right-hand side of (2.22) corresponds to a unit impulse function, as stated by the fundamental property of the delta function in (2.20).

Therefore, it is clear that the implicit weight factor from the varying speed of $\vec{k}(t)$ is equal to $\frac{1}{|\vec{k}'(\vec{k})|}$. Furthermore, by the Second Fundamental Theorem of Calculus:

$$\vec{k}(t)' = -\gamma \frac{d}{dt} \int_t^T \vec{G}(\tau) d\tau \quad (2.23)$$

$$= \gamma \frac{d}{dt} \int_T^t \vec{G}(\tau) d\tau \quad (2.24)$$

$$= \gamma \vec{G}(t) \quad (2.25)$$

The expression of the k -space pattern $p(\vec{k})$ is thus rewritten:

$$p(\vec{k}) = \int_0^T \frac{B_1^+(t)}{|\gamma \vec{G}(t)|} \left\{ {}^3\delta(\vec{k}(t) - \vec{k}) |\gamma \vec{G}(t)| \right\} dt \quad (2.26)$$

The term delimited by the curly braces in the integral is a normalized delta function describing the k -space trajectory; the full expression corresponding to the weighting of this trajectory is

$$W(\vec{k}(t)) = \frac{B_1^+(t)}{|\gamma \vec{G}(t)|} \quad (2.27)$$

Using the sifting property, (2.26) is rewritten

$$p(\vec{k}) = W(\vec{k}) \int_0^T \left\{ {}^3\delta(\vec{k}(t) - \vec{k}) |\gamma \vec{G}(t)| \right\} dt \quad (2.28)$$

$$= W(\vec{k}) S(\vec{k}) \quad (2.29)$$

The variable $W(\vec{k})$ defines the weighting factor over the full k -space: it is equal to $W(\vec{k}(t))$ everywhere $\vec{k}(t)$ is defined and undefined everywhere else. The variable $S(\vec{k})$ represents the unit weight trajectory that follows $\vec{k}(t)$. By replacing the inner integral of (2.19) by the new pattern variable $p(\vec{k})$,

$$m_r(\vec{x}) = j\gamma M_0 \int_{k_v} p(\vec{k}) e^{j\vec{k}\cdot\vec{x}} d\vec{k} \quad (2.30)$$

$$= j\gamma M_0 \mathcal{F}^{-1} \left\{ p(\vec{k}) \right\} \quad (2.31)$$

$$= j\gamma M_0 p(\vec{x}) \quad (2.32)$$

we see a very important relationship: the transverse magnetization resulting from an RF pulse $B_1^+(t)$ is simply the inverse Fourier transform of the k -space pattern $p(\vec{k})$ weighted by the tissue's magnetic properties, where $p(\vec{k})$ is related to the RF pulse by:

$$p(\vec{k}(t)) = \frac{B_1^+(t)}{|\gamma\vec{G}(t)|} \quad (2.33)$$

2.4 Parallel Transmission

Parallel transmission (pTx) is a type of selective excitation where the desired B_1^+ -field is generated by simultaneously exciting multiple RF coils, each of which exhibits an arbitrary but different sensitivity profile, with independently designed waveforms [13]. The central equation of parallel transmission consists of the superposition in space of the individual excitation pattern from each transmit coil to produce the desired excitation pattern $p_{des}(\vec{x})$:

$$p_{des}(\vec{x}) = \sum_{n=1}^N S_n(\vec{x}) p_n(\vec{x}) \quad (2.34)$$

Here, N is the number of independent coils, \vec{x} is the spatial coordinate vector and $S_n(\vec{x})$ and $p_n(\vec{x})$ are the sensitivity profile and excitation patterns of coil n , respectively. In discretized spatial coordinates, $p_{des}(\vec{x})$ can be thought of as a vector containing the values of the pattern at a finite number of voxels, M , defined over the FOX.

As shown in section 2.3, the excitation pattern is related to the gradient and RF coil waveforms through the k -space Fourier transform. For this reason, it is useful to express (2.34) in k -space:

$$p_{des}(\vec{k}) = \sum_{n=1}^N S_n(\vec{k}) * p_n(\vec{k}) \quad (2.35)$$

Similarly, in discretized k -space, $p_{des}(\vec{k})$ is a vector of M spatial frequency points that are traversed by the chosen k -space trajectory. In addition, the convolution in discretized notation amounts to a matrix/vector multiplication. The summation term on the right-hand side of (2.35) can be simplified to a single matrix and vector multiplication, where all sensitivity matrices $S_n(\vec{k})$ are grouped to form a single

matrix $S_{full}(\vec{k})$ and correspondingly, the individual $p_n(\vec{k})$ to a single vector $p_{full}(\vec{k})$.

$$p_{des}(\vec{k}) = \sum_{n=1}^N \left(\begin{bmatrix} S_{n1,1} & S_{n1,2} & \cdots & S_{n1,M/R} \\ S_{n2,1} & S_{n2,2} & \cdots & S_{n2,M/R} \\ \vdots & \vdots & \ddots & \vdots \\ S_{nM,1} & S_{nM,2} & \cdots & S_{nM,M/R} \end{bmatrix} \begin{bmatrix} p_{n1} \\ p_{n2} \\ \vdots \\ p_{nM/R} \end{bmatrix} \right) \quad (2.36)$$

$$= \begin{bmatrix} S_1 \\ \vdots \end{bmatrix} \begin{bmatrix} p_1 \\ \vdots \end{bmatrix} + \begin{bmatrix} S_2 \\ \vdots \end{bmatrix} \begin{bmatrix} p_2 \\ \vdots \end{bmatrix} + \cdots + \begin{bmatrix} S_N \\ \vdots \end{bmatrix} \begin{bmatrix} p_N \\ \vdots \end{bmatrix} \quad (2.37)$$

$$= \begin{bmatrix} S_1 \\ S_2 \\ \vdots \\ S_N \end{bmatrix} \begin{bmatrix} p_1 \\ p_1 \\ \vdots \\ p_1 \end{bmatrix} \quad (2.38)$$

$$= S_{full}(\vec{k}) p_{full}(\vec{k}) \quad (2.39)$$

The order in which the individual $S_n(\vec{k})$ and $p_n(\vec{k})$ are appended to $S_{full}(\vec{k})$ and $p_{full}(\vec{k})$ will not influence the outcome since it will only result in interchanging rows and columns. Equations 2.37 and 2.38 show one way of performing the concatenation. The factor R , present in the matrices element subscripts in equation 2.36, refers to a k -space trajectory reduction factor and will be explained shortly. Equation (2.39) is solved for $p_{full}(\vec{k})$ using well-known numerical techniques such as least-squares minimization algorithms and regularization techniques. The individual $p_n(\vec{k})$ are then simply extracted from the resulting $p_{full}(\vec{k})$.

Finally, the $B_{1n}(t)$ waveform for each independent coil n is found from (2.33) using the corresponding optimal k -space excitation profile $p_n(\vec{k})$:

$$B_{1n}(t) = \frac{p_n(\vec{k}(t))|\gamma G(t)|}{S(\vec{k}(t))} \quad (2.40)$$

Assuming the trajectory was chosen adequately to avoid aliasing, the unit weight sampling structure $S(\vec{k}(t))$ factor can be dropped. The mapping $\vec{k} \rightarrow t$ corresponds to the chosen k -space trajectory $\vec{k}(t)$. In other words, the value of the $B_{1n}(t)$ waveform at time point t is related to the weighting factor of the k -space pattern $p_n(\vec{k})$ at the k -space coordinates k that is traversed at time point t . The factor $|\gamma G(t)|$ compensates for the non-uniform k -space sampling density when the trajectory is non-Cartesian.

Parallel transmission provides many new degrees of freedom in designing RF pulses. Assuming each pattern $p_n(\vec{k})$ is defined for every point in the k -space trajectory, the system of equations in (2.39) becomes increasingly underdetermined as N increases. That is to say, there are more unknowns, specifically $(M \times N)$ unknowns, than constraining equations. One major application of pTx is the generation of

very complex excitation patterns such as spatially-selective multidimensional pulse patterns. These patterns are used for various purposes, such as volume selective excitation [12] and patient-induced B_1^+ inhomogeneities compensation [14]. However, the improved spatial resolution and pattern definition are accomplished at the expense of prolonged pulse duration, where the length of the pulse is contingent upon the desired k -space coverage, the sampling density and sampling rate.

Another approach is to introduce a reduction factor R in the k -space trajectory, where $R < N$. The mathematical framework of this pTx approach is analogous to the parallel imaging technique called sensitivity encoding (SENSE) [15] and thus is commonly referred to as transmit SENSE [13]. The scan duration of a receive coil is defined by the number of samples in its k -space trajectory and the sampling rate. By reducing the number of samples in the trajectory while maintaining k -space coverage, the scan duration is shortened and the image spatial resolution preserved. In standard imaging, the reduction in sampling density causes aliasing. In parallel imaging, each receive coil in the array acquires an aliased image weighted by its unique sensitivity signature. The aliased pixel contributions from each intermediate images are then unfolded back to their original positions by inversion of the corresponding coil's sensitivity matrix. In the context of transmission, an analogous concept is considered: the pulse duration can be shortened by reducing the number of samples while preserving the excitation pattern resolution. Here, the samples refer to the discretized points of the $B_{1n}(t)$ waveform. Each transmitting coil generates a pattern calculated from (2.39). The individual patterns $p_n(\vec{x})$ contain aliasing artifacts but the superposition of the contributing fields yields the desired $p_{des}(\vec{x})$. When

transmit SENSE is used to correct for B_1^+ -field non-uniformities, it is often referred to as “dynamic RF-shimming”.

As the reduction factor R is increased beyond N , the system of equations in (2.39) becomes overdetermined and there no longer exists an exact solution. Instead, minimization techniques are used to find the most optimal waveforms. Increasing deviation from the desired pattern is expected as R increases [4]. The asymptotical limit is given by the condition where the reduction factor is equal to the number of k -space pixels, M . In this situation, the entire k -space trajectory is reduced to a single sample. This case is often referred to as “static RF-shimming” since each element is excited with a different yet constant complex magnitude.

CHAPTER 3

Transmit Coil Simulation Models

The scope of our experiment is to design an RF coil for parallel excitation through simulations and establish the groundwork for future *in vivo* studies. The following sections lay out the specifications of the coil and describe the methods by which an accurate simulation model is generated.

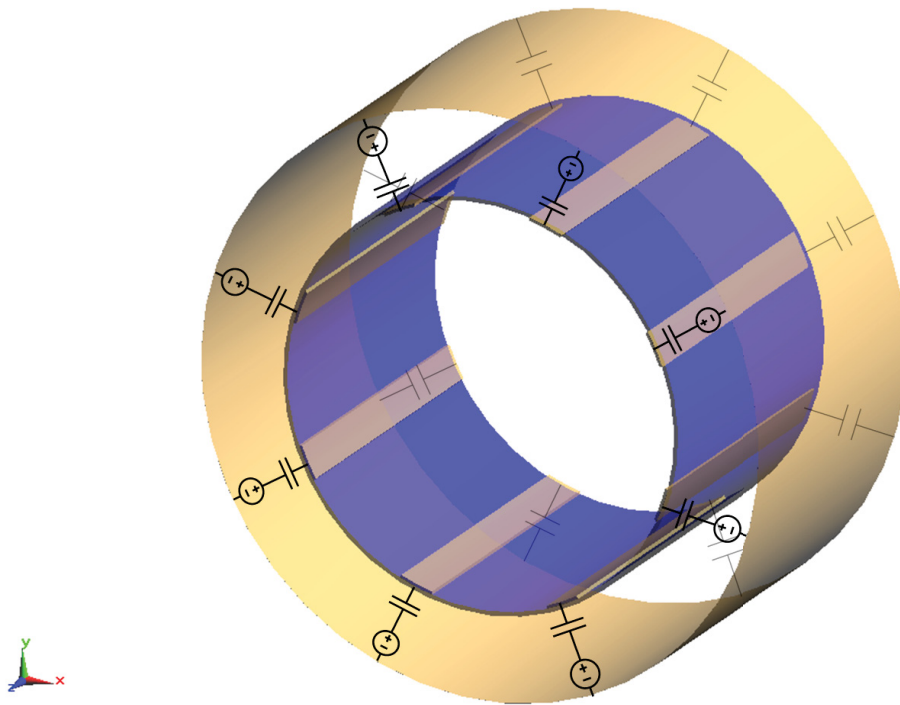
3.1 The TEM Resonator

MR excitation using parallel transmission relies on the premise that multiple, yet independent transmission coils simultaneously excite the FOX. The traditional transmission coil — the birdcage coil — is unable to generate independent excitations since the individual rung currents tightly couple to each other through the end-rings. The TEM resonator is another type of volume coil used for MR excitation. It was invented by Purcell for the very first NMR measurements in 1946 [16]. In the 1980s, the design was improved by Krause (1985) and Röschmann (1988) for human imaging. Through the recent works of Vaughan *et al* [17], it has reappeared over the last decade as a valuable alternative to the birdcage coil for its ability to operate efficiently at higher frequencies [7]. In addition to this, the multi-channel capabilities of the TEM resonator makes it the prevailing coil design used in parallel transmission applications.

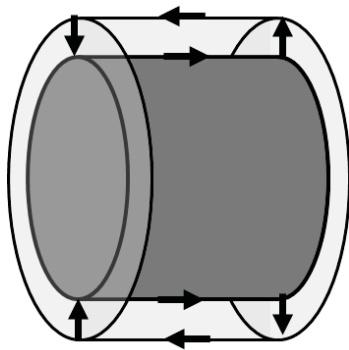
Similar to the traditional birdcage coil, the TEM resonator is composed of multiple axially oriented rungs laid out in a circle. Each rung, or line element, connects

on either end to the outer cylindrical shield through capacitive elements, as shown in Figure 3–1a. In this arrangement, the current driven into one element returns by the shield making the current path through each element practically independent of one another. This current flow is illustrated in Figure 3–1b. In fact, the resonance of the coil directly relates to the resonance of one element and a portion of the shield, as shown in Figure 3–1c. The currents in the line elements are for the most part directed along the main axis of the coil and propagate primarily in the transverse electromagnetic (TEM) mode — hence, the name TEM resonator.

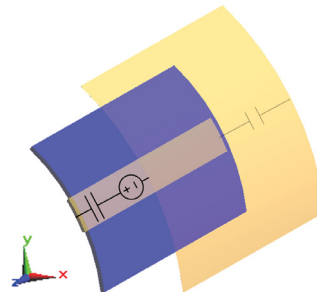
Coil specifications, such as coil geometry and operability, are determined while taking into account high-field MRI system availability, compatibility and patient comfort. The target operating frequency of the TEM resonator model is chosen to be 300 MHz, the Larmor frequency of hydrogen subject to a 7T magnetic field. Although successful MRI system designs have surpassed magnetic field strengths of 11T, 7T MRI systems have become the standard for high-field imaging due to the optimal balance between the signal-to-noise ratio and the size of the bore [18]. Additionally, a second coil model of identical geometry is designed to operate at 128 MHz (3T). This coil will provide a point of reference to standard clinical field strength imaging, where B_1 -field inhomogeneities are known to be negligible. The coil models are equipped with 8 independent line elements. A maximum number of line elements is desirable in order to achieve maximal controllability of the B_1^+ -field. However, for design complexity reasons, most MRI systems equipped for parallel transmission today are fitted with only 8 independent RF drive ports.



(a)



(b)



(c)

Figure 3-1: The TEM resonator: (a) the model of the an 8-element coil with the end-capacitors and sources, (b) the current flow diagram and (c) the single-element building block of the TEM resonator.

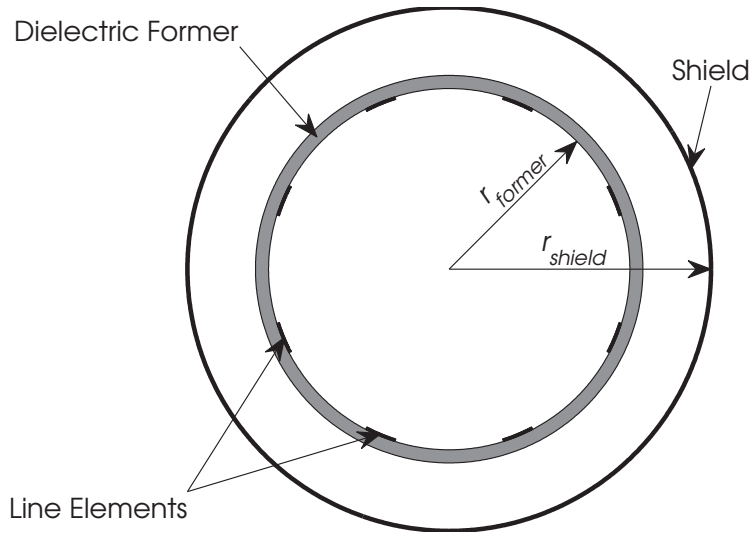


Figure 3-2: The cross-sectional schematic of the TEM resonator.

Figure 3-2 shows the cross-sectional geometry of the TEM resonator. The dimensions are selected in accordance with standard adult head coil sizes. The shield has an inner radius, r_{shield} , of 190 mm and is made of 35- μm -thick copper sheet. A cylindrical dielectric former of 130 mm inner radius (r_{former}) and 2.8 mm thickness is placed coaxially within the shield. Eight copper-sheet line elements conform to the inner wall of the former. The length of the coil is 200 mm. The end-capacitor values and the width and thickness of the line elements are adjusted to achieve the desired coil resonance.

3.2 MTL Model

Several works have shown that the TEM resonator behaves very much like a multi-conductor transmission line (MTL) terminated by capacitive loads [19][20]. The MTL model of the coil can estimate important coil parameters such as the input impedance, the S_{11} parameter and the electromagnetic field distributions. These estimations agree very closely to full-wave three-dimensional electromagnetic analysis calculations, yet are achieved with significantly less computing power. During design phase, the transmission line model provides a way to quickly understand the effects of model parameters and allows for faster design turn-overs. Once the desired behaviour is achieved, the MTL model is mapped to a three-dimensional model and solved using computational electrodynamic analysis techniques for greater precision and design confidence.

Transmission line theory is based on the fundamental assumption that the fields in a transmission line propagate in the transverse electromagnetic (TEM) mode. The TEM mode simply implies that the electric and magnetic field components in the direction of propagation are zero. The direction of propagation is conventionally assigned to the z -axis, and the transverse components to the xy -plane. In order to be consistent with the TEM structure, the conductors of the transmission line must be *perfect*; otherwise, conduction losses along the length of the z -axis will result in changes in E_z , as depicted in Figure 3–3. The transmission line must also be *uniform along the direction of propagation*. In other words, the cross-sectional geometry and electromagnetic properties of the dielectrics and conductors must not vary with z .

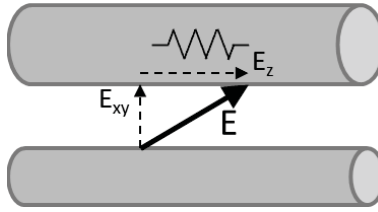


Figure 3–3: The electric field resulting from conduction losses along the length of two parallel waveguides.

The TEM resonator satisfies the requirements for TEM structure: the line elements and the shield are made from very conductive material and the cross-section of the coil does not vary along its length. The following sections explain how an MTL model is created for the TEM resonator and how it is used to determine the important electrical properties of the coil.

3.2.1 MTL Equations

The transmission line equations formulate the waveguide problem in terms of circuit theory terms. Since the EM fields have no z component in TEM mode, Maxwell’s equations in the transverse plane simplify to those of electrostatics. This implies that current and voltage can be uniquely defined in the transverse plane. Moreover, since the transmission line is uniform along z , the electrostatics at any given cross-section are sufficient to describe the electrostatics throughout the entire coil.

The first set of transmission line equations describes the per-unit-length (PUL) voltage on each conductor with respect to position z . Changes in voltage on the i -th conductor are caused by *i*) resistive losses from the current I_i flowing through the non-ideal conductor i and reference conductor; and *ii*) induced voltage by time-varying magnetic fields emanating from neighbouring conductors. These effects are

summarized by the following equation:

$$\begin{aligned} \frac{\partial V_i(z, t)}{\partial z} = & - [r_{i1}I_1(z, t) + \cdots + r_{ii}I_i(z, t) + \cdots + r_{iN}I_N(z, t)] \\ & - \frac{d}{dt} [l_{i1}I_1(z, t) + \cdots + l_{ii}I_i(z, t) + \cdots + l_{iN}I_N(z, t)] \end{aligned} \quad (3.1)$$

where V_i is the voltage between conductor i and the reference conductor (in volts); I_i is the current on conductor i (in amperes); r_{ij} and l_{ij} are the PUL resistance (in ohms) and inductance (in henries) between conductors i and j , respectively; and N is the number of conductors in the transmission line. A thorough derivation of Equation 3.1 from Maxwell's equations can be found in the appendix in Section A.2. The set of N voltage equations are more easily expressed in matrix/vector form:

$$\frac{\partial \mathbf{V}(z, t)}{\partial z} = -(\mathbf{R} + \frac{d}{dt}\mathbf{L})\mathbf{I}(z, t) \quad (3.2)$$

$$(3.3)$$

where the vectors $\mathbf{V}(z, t)$ and $\mathbf{I}(z, t)$ are the reference voltages and the currents on the N conductors, respectively; and the matrices \mathbf{R} and \mathbf{L} , defined as:

$$\mathbf{R} = \begin{bmatrix} r_{11} & r_{12} & \cdots & r_{1N} \\ r_{21} & r_{22} & \cdots & r_{2N} \\ \vdots & \vdots & \ddots & \vdots \\ r_{N1} & r_{N2} & \cdots & r_{NN} \end{bmatrix} \quad \text{and} \quad \mathbf{L} = \begin{bmatrix} l_{11} & l_{12} & \cdots & l_{1N} \\ l_{21} & l_{22} & \cdots & l_{2N} \\ \vdots & \vdots & \ddots & \vdots \\ l_{N1} & l_{N2} & \cdots & l_{NN} \end{bmatrix} \quad (3.4)$$

are the PUL resistance and inductance matrices of the transmission line, respectively.

The second set of transmission line equations describes the per-unit-length current on each conductor with respect to position z . Changes in current on the i -th

conductor are caused by *i*) conduction currents from lossy dielectrics between conductor *i* and the neighbouring conductors; and *ii*) displacement currents from bounded charges in the dielectric between conductor *i* and the neighbouring conductors. These effects are summarized by the following equation:

$$\begin{aligned} \frac{\partial I_i(z, t)}{\partial z} = & - [g_{i1}V_{i1}(z, t) + \cdots + g_{ii}V_{ii}(z, t) + \cdots + g_{iN}V_{iN}(z, t)] \\ & - \frac{d}{dt} [c_{i1}V_{i1}(z, t) + \cdots + c_{ii}V_{ii}(z, t) + \cdots + c_{iN}V_{iN}(z, t)] \end{aligned} \quad (3.5)$$

where g_{ij} and c_{ij} are the PUL conductance (in siemens) and capacitance (in farads) between conductors *i* and *j*, respectively; V_{ij} is the voltage between conductors *i* and *j*, for $i \neq j$; and V_{ii} is the voltage between conductor *i* and the reference conductor. A thorough derivation of Equation 3.5 from Maxwell's equations can be found in Section A.1. Note that the voltages in Equation 3.5 are line voltages, whereas the voltages in Equation 3.1 are in reference to the reference conductor. Rewriting Equation 3.5 in terms of reference conductor voltages gives:

$$\begin{aligned} \frac{\partial I_i(z, t)}{\partial z} = & - \left[-g_{i1}V_1(z, t) + \cdots + \sum_{k=1}^N g_{ik}V_k(z, t) + \cdots - g_{iN}V_N(z, t) \right] \\ & - \frac{d}{dt} \left[-c_{i1}V_1(z, t) + \cdots + \sum_{k=1}^N c_{ik}V_k(z, t) + \cdots - c_{iN}V_N(z, t) \right] \end{aligned} \quad (3.6)$$

The set of N current equations expressed in matrix/vector form is:

$$\frac{\partial \mathbf{I}(z, t)}{\partial z} = -(\mathbf{G} + \frac{d}{dt}\mathbf{C})\mathbf{V}(z, t) \quad (3.7)$$

where the vectors $\mathbf{V}(z, t)$ and $\mathbf{I}(z, t)$ are the reference voltages and the currents on the N conductors, respectively; and the matrices \mathbf{G} and \mathbf{C} , defined as:

$$\mathbf{G} = \begin{bmatrix} \sum_{k=1}^N g_{1k} & -g_{12} & \cdots & -g_{1N} \\ -g_{21} & \sum_{k=1}^N g_{2k} & \cdots & -g_{2N} \\ \vdots & \vdots & \ddots & \vdots \\ -g_{N1} & -g_{N2} & \cdots & \sum_{k=1}^N g_{Nk} \end{bmatrix} \quad (3.8)$$

and

$$\mathbf{C} = \begin{bmatrix} \sum_{k=1}^N c_{1k} & -c_{12} & \cdots & -c_{1N} \\ -c_{21} & \sum_{k=1}^N c_{2k} & \cdots & -c_{2N} \\ \vdots & \vdots & \ddots & \vdots \\ -c_{N1} & -c_{N2} & \cdots & \sum_{k=1}^N c_{Nk} \end{bmatrix} \quad (3.9)$$

are the PUL conductance and capacitance matrices of the transmission line, respectively.

3.2.2 Poisson's Equations

In order to calculate the PUL parameters of the coil, the electric and magnetic field distributions are needed. Maxwell's equations in point-form are:

$$\text{Faraday's Law of Induction:} \quad \nabla \times \vec{E} = -j\omega\mu\vec{H} \quad (3.10)$$

$$\text{Ampère's Circuital Law:} \quad \nabla \times \vec{H} = \sigma\vec{E} + j\omega\varepsilon\vec{E} + \mathbf{J}_i \quad (3.11)$$

$$\text{Gauss's Law:} \quad \nabla \cdot \vec{D} = \rho_{free} \quad (3.12)$$

$$\text{Gauss's Law for Magnetism:} \quad \nabla \cdot \vec{B} = 0 \quad (3.13)$$

where \vec{E} , \vec{D} , \vec{H} and \vec{B} are the electric field intensity (in volts per meter), electric flux density (in coulombs per square meter), magnetic field intensity (in amperes per meter) and magnetic flux density (in teslas), respectively; μ , σ and ε are the medium's permeability (in webers per ampere per meter), conductivity (in siemens per meter) and permittivity (in farads per meter), respectively; ρ_{free} is the free charge density (in coulombs per cube meter) and \vec{J}_i (in amperes per square meter) is the impressed current density. Since $E_z = 0$ and $H_z = 0$ under TEM regime, Equations 3.10 and 3.11 can be rewritten as:

$$(\nabla_t + \nabla_z) \times \vec{E}_t = \underbrace{(\nabla_z \times \vec{E}_t)}_{\text{transverse component}} + \underbrace{(\nabla_t \times \vec{E}_t)}_{\text{z-component}} = \underbrace{-j\omega\mu\vec{H}_t}_{\text{transverse component}} \quad (3.14)$$

$$(\nabla_t + \nabla_z) \times \vec{H}_t = \underbrace{(\nabla_z \times \vec{H}_t)}_{\text{transverse component}} + \underbrace{(\nabla_t \times \vec{H}_t)}_{\text{z-component}} = \underbrace{\sigma\vec{E}_t + j\omega\varepsilon\vec{E}_t}_{\text{transverse component}} + \underbrace{\vec{J}_i}_{\text{z-component}} \quad (3.15)$$

where the subscripts t and z designate the transverse plane and z -axis components, respectively. Hence, we can deduce from Equations 3.14 and 3.15 that $\nabla_t \times \vec{E}_t$ is always zero and $\nabla_t \times \vec{H}_t = \vec{J}_i$.

By the fundamental theorem of vector calculus, any vector field \vec{F} decomposes into an irrotational (curl-free) component, $\vec{F}_{irr} = -\nabla\phi$, and a solenoidal (divergence-free) component, $\vec{F}_{sol} = \nabla \times \vec{A}$. The scalar field ϕ and vector field \vec{A} are often called the *scalar potential* and *vector potential* of \vec{F} , respectively. Since $\nabla \times \vec{E}_t = 0$, \vec{E}_t is a curl-free field and can be fully defined in terms of a scalar potential:

$$\vec{E}_t = -\nabla V \quad (3.16)$$

The scalar potential of an electric field is the electric potential — or simply, the voltage (in volts). By Gauss’s law and by safely assuming that no free charges can exist in the media surrounding the conductors, the following equation must always hold under TEM conditions:

$$\nabla \cdot \varepsilon \nabla V = 0 \tag{3.17}$$

Equation 3.17 is a special 2D elliptic partial differential equation (PDE) known as Poisson’s equation. By setting up voltage boundary conditions on all the conductors, the voltage potential in the 2D space surrounding the conductors, $V(x, y)$, can be solved using a numerical approach such as the finite-element method (FEM) or the method of moments (MoM). Since the region of interest is a bounded domain enclosed by the shield conductor, the FEM is well-suited for our PDE problem. From the solution $V(x, y)$, the electric field $\vec{E}_t(x, y)$ in the area around the conductors is calculated from Equation 3.16.

By Gauss’s law of magnetism, \vec{H}_t is a divergence-free field, thus can be fully defined in terms of a vector potential, \vec{A} (in volt-seconds per meter):

$$\vec{H}_t = \frac{1}{\mu} \nabla \times \vec{A} \tag{3.18}$$

By vector identity, the curl of \vec{H}_t is:

$$\nabla \times \vec{H}_t = \frac{1}{\mu} \nabla \times \nabla \times \vec{A} = \frac{1}{\mu} \nabla(\nabla \cdot \vec{A}) - \vec{\nabla}^2 \vec{A} \tag{3.19}$$

Note that $\vec{\nabla}^2$ is the vector Laplacian operator and operates on the vector field \vec{A} as $\vec{\nabla}^2 \vec{A} = \nabla^2 A_x \hat{i} + \nabla^2 A_y \hat{j} + \nabla^2 A_z \hat{k}$ where ∇^2 is the scalar Laplacian operator. For

simplicity, the magnetic vector potential is chosen to be fully solenoidal so that the term $(\nabla \cdot \vec{A})$ in Equation 3.19 disappears. The z -component of Equation 3.15 is rewritten in terms of the magnetic vector potential:

$$\nabla_t \times \vec{H}_t = -\frac{1}{\mu} \nabla^2 A_z = J_i \quad (3.20)$$

This equation implies that, outside of the conductors, where $J_i = 0$, the z -component of the magnetic potential also follows a Poisson's equation:

$$\nabla \cdot \frac{1}{\mu} \nabla A_z = 0 \quad (3.21)$$

Similarly to the electric potential, Equation 3.21 can be solved for $A_z(x, y)$ by FEM for a set of magnetic potential boundary conditions on the conductors. The magnetic field distribution is then calculated as:

$$\begin{aligned} \vec{H}_t &= \frac{1}{\mu} \left[\left(\frac{\partial A_z}{\partial y} - \frac{\partial A_y}{\partial z} \right) \hat{i} + \left(\frac{\partial A_x}{\partial z} - \frac{\partial A_z}{\partial x} \right) \hat{j} \right] \\ &= \frac{1}{\mu} \left[\frac{\partial A_z}{\partial y} \hat{i} - \frac{\partial A_z}{\partial x} \hat{j} \right] \end{aligned} \quad (3.22)$$

Note that the partial derivatives $\frac{\partial A_x}{\partial z}$ and $\frac{\partial A_y}{\partial z}$ are necessarily zero since the magnetic field should not vary with respect to z in the TEM structure.

The commercially available PDE toolbox from Mathworks provides a powerful and flexible FEM platform for solving and visualizing PDE problems. The geometry of the coil cross-section is defined through disjointed 2D regions representing the different dielectrics of the problem. Using the toolbox's meshing routine, the regions are discretized into smaller triangular sub-regions, called finite elements. The general

elliptic PDE:

$$-\nabla \cdot c \nabla U + aU = f \quad (3.23)$$

where U is the unknown potential variable and c , a and f are the PDE coefficients, is discretized on each triangle node. When solving for the electric potential, the coefficient c is set to the permittivity corresponding to each node; in the case of the magnetic potential, c is set to the inverse of the permeability at each node. In both cases, the PDE coefficients a and f are set to zero for all nodes. The system of node equations is then solved numerically for a given set of boundary conditions. The electric and magnetic fields are then calculated from Equations 3.16 and 3.22, respectively.

3.2.3 Per Unit Length Parameters

The PUL capacitance \mathbf{C} , conductance \mathbf{G} , inductance \mathbf{L} and resistance \mathbf{R} matrices capture specific information about how the electromagnetic fields behave in a given transmission line. By setting up strategic boundary conditions, the coefficients of the parameter matrices are determined from the solutions to the electric and magnetic Poisson equations.

PUL Capacitance. The capacitance matrix \mathbf{C} models the PUL displacement current flowing between the conductors of the transmission line. Although the MTL equations from Equations 3.2 and 3.7 are expressed in terms of reference voltages, displacement currents in the transmission line are more easily analysed in terms of line voltages. By examining Equation 3.5, the PUL displacement current flowing out

of the i -th conductor, $I_{d,i}$, is:

$$\frac{\partial I_{d,i}}{\partial z} = -\frac{d}{dt} [c_{i1}V_{i1}(z,t) + \cdots + c_{ii}V_{ii}(z,t) + \cdots + c_{iN}V_{iN}(z,t)] \quad (3.24)$$

The displacement current strictly between conductors i and j is:

$$\frac{\partial I_{d,i}}{\partial z} = -\frac{d}{dt} c_{ij} V_{ij} \quad (3.25)$$

where the potential differences V_{ik} in Equation 3.24 were forced to zero for all $k \neq j$.

By combining this result to the definition of PUL capacitance from Equation A.22, c_{ij} is:

$$\begin{aligned} c_{ij} &= \frac{q_i}{V_{ij}} \Big|_{V_{ik}=0 \text{ for } k \neq j} \\ &= \varepsilon \frac{\oint_c \vec{E} \cdot \hat{n} dl}{-\int_{c'} \vec{E} \cdot d\vec{l}} \Big|_{V_{ik}=0 \text{ for } k \neq j} \end{aligned} \quad (3.26)$$

where q_i is the total PUL charge on the i -th conductor (in coulombs); c is a path around the i -th conductor; and c' is a path from conductor j to i . When computing c_{ij} , the boundary conditions to Poisson's Equation 3.17 must respect the line voltages prescribed in Equation 3.26. In other words,

$$\begin{aligned} V &= V_0, \text{ on the } j\text{-th conductor} \\ V &= 0V, \text{ on all other conductors, including the shield} \end{aligned} \quad (3.27)$$

as shown in Figure 3-4. Each entry of the i -th row is determined by solving the electric potential $V(x, y)$ from Poisson's Equation 3.17 with the boundary conditions

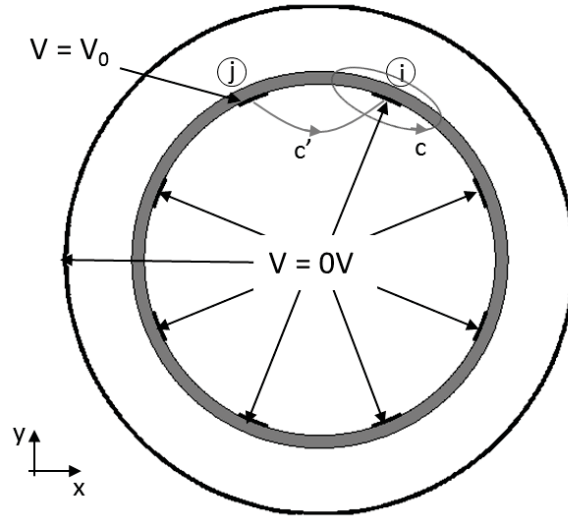


Figure 3–4: The cross-section of the TEM resonator annotated with the path c around the i -th conductor; the path c' from conductor j to i ; and the Poisson boundary conditions prescribed in Equation 3.26

in Equation 3.27 for $j = 1..8$, and computing $\vec{E}(x, y)$ from Equation 3.16. Alternatively, since capacitance is a reciprocal property, it is sufficient to solve Poisson's equation over one set of boundary conditions for the entire row:

$$V = V_0, \text{ on the } i\text{-th conductor boundaries}$$

$$V = 0V, \text{ on all other conductor boundaries, including the shield} \quad (3.28)$$

and infer c_{ij} from c_{ji} . The self-capacitance c_{ii} is calculated implicitly from Equation 3.5 where $V_{ij} = V_0$ for all $j = 1 \dots 8$:

$$\begin{aligned} \frac{\partial I_i}{\partial z} &= -\frac{d}{dt} [c_{i1}V_{i1}(z, t) + \dots + c_{ii}V_{ii}(z, t) + \dots + c_{iN}V_{iN}(z, t)] \\ &= -\frac{d}{dt} V_0 \sum_{k=1}^N c_{1k} \end{aligned} \quad (3.29)$$

By placing the path c around the i -th conductor, the result from Equation 3.26 is simply the sum of the capacitances of the i -th row, $\sum_{k=1}^N c_{1k}$. The remaining rows of \mathbf{C} can be calculated by applying the boundary conditions from 3.28 in turn to each line element. In the case of the TEM resonator, where the line elements are identical and uniformly spaced, the capacitance matrix is circulant. Therefore, the entries of the first row are sufficient to calculate the full matrix.

PUL Conductance. Dielectric losses are modelled through the conductance matrix \mathbf{G} . These losses represent conduction currents between neighbouring conductors and losses from polarization of bounded charges. The conduction currents are accounted for by the material's conductivity, σ , whereas the polarization losses are usually modelled as an imaginary component ε_b to the permittivity: $\varepsilon = \varepsilon' - j\varepsilon_b$. Ampère's law from Equation 3.11 is rewritten to combine ε_b and σ into a single

permittivity value $\hat{\varepsilon}$:

$$\begin{aligned}
\nabla \times \vec{H} &= \sigma \vec{E} + j\omega \varepsilon \vec{E} + J_i \\
&= (\sigma + j\omega(\varepsilon' - j\varepsilon_b)) \vec{E} + J_i \\
&= j\omega(\varepsilon' - j(\frac{\sigma}{\omega} + \varepsilon_b)) \vec{E} + J_i \\
&= j\omega \hat{\varepsilon} \vec{E} + J_i
\end{aligned} \tag{3.30}$$

where $\hat{\varepsilon}(\omega) = (\varepsilon' - j\frac{\omega\varepsilon_b + \sigma}{\omega})$. Using the complex permittivity in place of ε in Poisson's equation 3.17, a special capacitance matrix $\hat{\mathbf{C}}$ can be calculated to include both PUL capacitances and PUL dielectric losses. The matrices \mathbf{C} and \mathbf{G} are recovered from $\hat{\mathbf{C}}$ through:

$$\mathbf{C} = \Re\{\hat{\mathbf{C}}\} \tag{3.31}$$

$$\mathbf{G} = -\omega \Im\{\hat{\mathbf{C}}\} \tag{3.32}$$

Note that by assuming that no free charges exist in the dielectric media, it is implied that σ is zero and that $\hat{\varepsilon}$ does not vary with ω . Therefore, the matrices \mathbf{C} and \mathbf{G} are constant with respect to frequency.

PUL Inductance. The PUL inductance models the induced voltage on a conductor by the time-varying currents from neighbouring conductors. By examining Equation 3.1, the PUL induced voltage on the i -th conductor is:

$$\frac{\partial V_{d,i}}{\partial z} = -\frac{d}{dt} [l_{i1}I_1 + \dots + l_{ii}I_i + \dots + l_{iN}I_N] \tag{3.33}$$

Unlike the calculations for c_{ij} and g_{ij} , l_{ij} cannot be isolated in Equation 3.33 by simply setting the currents I_k to zero for all $k \neq j$. The magnetic Poisson equation

3.21 allows only for direct control over the magnetic potential on the conductor boundaries. Therefore, a few more steps are required to solve for \mathbf{L} . The magnetic potential $A_{z,i}(x, y)$ is calculated by solving the magnetic Poisson equation for the following boundary conditions:

$$\begin{aligned} A_z &= \psi_0, \text{ on the } i\text{-th conductor boundaries} \\ A_z &= 0, \text{ on all other conductor boundaries, including the shield} \end{aligned} \quad (3.34)$$

and the magnetic field distribution $\vec{H}_{t,i}(x, y)$ is calculated using Equation 3.22. From the definition of current in Equation A.6b, we can calculate the currents on each conductor due to the magnetic potential boundary conditions in Equation 3.34. These induction currents fill the i -th row of the current distribution matrix $\tilde{\mathbf{I}}$:

$$\tilde{\mathbf{I}} = \begin{bmatrix} \tilde{i}_{11} & \tilde{i}_{12} & \cdots & \tilde{i}_{1N} \\ \tilde{i}_{21} & \tilde{i}_{22} & \cdots & \tilde{i}_{2N} \\ \vdots & \vdots & \ddots & \vdots \\ \tilde{i}_{N1} & \tilde{i}_{N2} & \cdots & \tilde{i}_{NN} \end{bmatrix} \quad (3.35)$$

where \tilde{i}_{ij} reads as the *current on conductor j due to $A_z = \psi_0$ on conductor i and $A_z = \psi_0$ on all other conductors*. Once again, since all the line elements are identical and uniformly spaced, the matrix $\tilde{\mathbf{I}}$ is circulant and can be filled in with one set of boundary conditions.

The currents relate to the total PUL flux between the j -th conductor and the shield by the PUL inductances:

$$\psi_{ij} = \tilde{i}_{i1}l_{j1} + \cdots + \tilde{i}_{ij}l_{jj} + \cdots + \tilde{i}_{iN}l_{jN} \quad (3.36)$$

where ψ_{ij} reads as the *total PUL flux between conductor j and the shield due to currents from $A_z = \psi_0$ on conductor i and $A_z = \psi_0$ on all other conductors*. In matrix notation,

$$\mathbf{\Psi} = \mathbf{L}\tilde{\mathbf{I}}^T \quad (3.37)$$

The PUL flux between the i -th line element and the shield, ψ_i (in webers), is:

$$\psi_i = \mu \int_{c'} \vec{H} \cdot \hat{n} dl \quad (3.38)$$

where c' is a path from conductor i to the shield. The coefficients of $\mathbf{\Psi}$ can be calculated from the magnetic field distribution using Equation 3.38. However, it is quickly realized that the flux ψ_{ij} corresponds simply to the magnetic potential difference between the conductor i and the shield. Therefore, the PUL flux matrix is:

$$\mathbf{\Psi} = \begin{bmatrix} \psi_{11} & \psi_{12} & \cdots & \psi_{1N} \\ \psi_{21} & \psi_{22} & \cdots & \psi_{2N} \\ \vdots & \vdots & \ddots & \vdots \\ \psi_{N1} & \psi_{N2} & \cdots & \psi_{NN} \end{bmatrix} = \begin{bmatrix} \psi_0 & 0 & \cdots & 0 \\ 0 & \psi_0 & \cdots & 0 \\ \vdots & \vdots & \ddots & \vdots \\ 0 & 0 & \cdots & \psi_0 \end{bmatrix} \quad (3.39)$$

and the PUL inductance matrix of the transmission line is:

$$\mathbf{L} = \psi_0 \tilde{\mathbf{I}}^{-1} \quad (3.40)$$

PUL Resistance. The PUL resistance accounts for resistive losses from the line elements and shield. For applications operating in high frequency ranges such as MRI coils, the resistance matrix most accurately models the transmission line losses

by satisfying the power dissipation relation [20]:

$$P(z) = \frac{1}{2} \mathbf{I}(z) \mathbf{R} \mathbf{I}(z)^T \quad (3.41)$$

The total power dissipated in the volume of a coil per unit length, P (in watts), is:

$$\begin{aligned} P &= \frac{1}{2} \iint_S \vec{E} \cdot \vec{J}^* dA \\ &= \frac{1}{2} \iint_S \rho \vec{J}^2 dA \\ &= \frac{1}{2} \oint_{\partial S} R_s J_s^2 dl \end{aligned} \quad (3.42)$$

where ρ and J are the resistivity (in ohm-meters) and current density (in amperes per square meter), respectively; R_s and J_s are the surface resistivity and surface current density (in amperes per meter), respectively; S is the cross-sectional area of the conductors and ∂S is the collection of contours around each conductor. For a given magnetic field distribution $\vec{H}_{t,i}(x, y)$, the surface current density distribution J_s on all conductor boundaries is easily determined. Recall that the current on a conductor and its surface current density are related by:

$$I = \oint_c J_s dl \quad (3.43)$$

where c is the contour of the conductor. Comparing this equation and the definition of current in Equation A.6b implies that:

$$J_s = H_{t,tan} \quad (3.44)$$

where $H_{t,tan}$ is the transverse magnetic field tangent to the conductor boundary. The PUL power dissipation matrix $\tilde{\mathbf{P}}$ is defined as:

$$\tilde{\mathbf{P}} = \frac{1}{2} \tilde{\mathbf{I}} \mathbf{R} \tilde{\mathbf{I}}^T \quad (3.45)$$

where

$$\tilde{P}_{ij} = \begin{bmatrix} \tilde{i}_{i1} & \tilde{i}_{i2} & \cdots & \tilde{i}_{iN} \end{bmatrix} \begin{bmatrix} \mathbf{R} \end{bmatrix} \begin{bmatrix} \tilde{i}_{j1} \\ \tilde{i}_{j2} \\ \vdots \\ \tilde{i}_{jN} \end{bmatrix} \quad (3.46)$$

Also, from the definition of ohmic power dissipation, the elements $\tilde{\mathbf{P}}$ are also equal to:

$$P_{ij} = \frac{1}{2} \oint_l R_s J_{s,i} J_{s,j} dl \quad (3.47)$$

where $J_{s,i}$ is the current density distribution on the conductors resulting from $A_z = \psi_0$ on conductor i and $A_z = \psi_0$ on all other conductors. Although the off-diagonal coefficients of $\tilde{\mathbf{P}}$ do not physically equal to power, the equality between Equations 3.46 and 3.47 must still hold for all ij . Therefore, the matrix \mathbf{R} is computed by:

$$\mathbf{R} = 2\tilde{\mathbf{I}}^{-1} \tilde{\mathbf{P}} (\tilde{\mathbf{I}}^T)^{-1} \quad (3.48)$$

3.2.4 Model Measurements

Once the transmission line parameters of the TEM resonator are determined, the voltage and current of each line element can be calculated at any position along the length of the coil. By calculating the voltage and current at the ends of the

line elements, the line elements and shield are regarded as a "black box". The remaining components of the coil, such as the end capacitors and the drive circuit, assemble around the black box as lumped elements. The resulting circuit model allows for measuring important electrical characteristics of the coil when it is subject to harmonic stimuli.

Voltage and current are tightly coupled through the transmission line equations, where one quantity is proportional to the z -derivative of the other. In order to decouple voltage and current, the two sets of transmission line equations are incorporated into a single matrix/vector expression. Since MRI coils operate primarily with harmonic signals, the transmission line equations are conventionally expressed in the frequency domain in terms of the complex Laplace argument s :

$$\frac{\partial}{\partial z} \begin{bmatrix} \mathbf{V}(z, s) \\ \mathbf{I}(z, s) \end{bmatrix} = (\mathbf{D} + s\mathbf{E}) \begin{bmatrix} \mathbf{V}(z, s) \\ \mathbf{I}(z, s) \end{bmatrix} \quad (3.49)$$

where

$$\mathbf{D} = \begin{bmatrix} 0 & -\mathbf{R} \\ -\mathbf{G} & 0 \end{bmatrix} \quad \text{and} \quad \mathbf{E} = \begin{bmatrix} 0 & -\mathbf{L} \\ -\mathbf{C} & 0 \end{bmatrix}$$

Equation 3.49 is a ordinary differential equation with the following solution:

$$\begin{bmatrix} \mathbf{V}(z, s) \\ \mathbf{I}(z, s) \end{bmatrix} = e^{(\mathbf{D}+s\mathbf{E})z} \mathbf{A} \quad (3.50)$$

The constant matrix \mathbf{A} is determined by setting z to 0:

$$\begin{bmatrix} \mathbf{V}(0, s) \\ \mathbf{I}(0, s) \end{bmatrix} = e^{(\mathbf{D}+s\mathbf{E}) \cdot 0} \mathbf{A} = \mathbf{A} \quad (3.51)$$

Therefore, the current and voltage solution is:

$$\begin{bmatrix} \mathbf{V}(z, s) \\ \mathbf{I}(z, s) \end{bmatrix} = e^{(\mathbf{D}+s\mathbf{E})z} \begin{bmatrix} \mathbf{V}(0, s) \\ \mathbf{I}(0, s) \end{bmatrix} \quad (3.52)$$

where $\mathbf{V}(0, s)$ and $\mathbf{I}(0, s)$ are the boundary conditions at the input of the line elements.

The line elements and the shield are regarded in circuit theory terms as a 16-port network, as depicted in Figure 3-5. The voltage and current at the ports of the

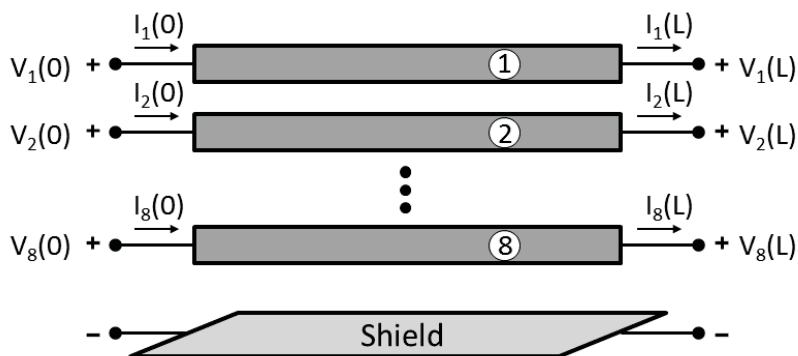


Figure 3-5: A 16-port network representation of the line elements and shield.

network are related by the chain parameters $\Phi(s)$:

$$\begin{aligned} \begin{bmatrix} \mathbf{V}(L, s) \\ \mathbf{I}(L, s) \end{bmatrix} &= \Phi(s) \begin{bmatrix} \mathbf{V}(0, s) \\ \mathbf{I}(0, s) \end{bmatrix} \\ &= \begin{bmatrix} \Phi_{11}(s) & \Phi_{12}(s) \\ \Phi_{21}(s) & \Phi_{22}(s) \end{bmatrix} \begin{bmatrix} \mathbf{V}(0, s) \\ \mathbf{I}(0, s) \end{bmatrix} \end{aligned} \quad (3.53)$$

where $\Phi(s) = e^{(\mathbf{D}+s\mathbf{E})L}$ and L is the length of the coil. The end capacitors on the load-side of the coil, i.e. at $z = L$, connect between the line elements and the shield, as depicted in Figure 3–6. The port currents relate to the port voltages in terms of

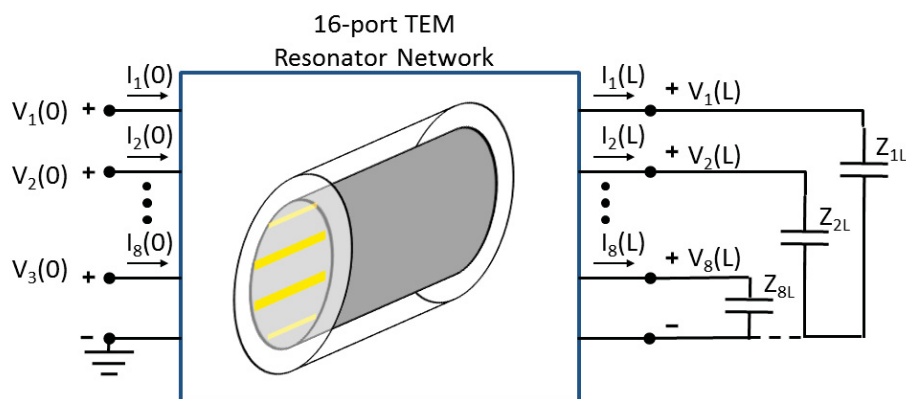


Figure 3–6: The TEM resonator network connected to the load-side capacitors Z_{iL} , for $i = 1 \dots 8$.

the impedance. On the load side,

$$V_1(L, s) = Z_{1L}I_1(L, s)$$

$$V_2(L, s) = Z_{2L}I_2(L, s)$$

...

$$V_8(L, s) = Z_{8L}I_8(L, s)$$

or equivalently,

$$\mathbf{V}(L, s) = \mathbf{Z}_L\mathbf{I}(L, s) \quad (3.54)$$

where \mathbf{Z}_L is a diagonal matrix with $Z_{L,ii} = Z_{iL}$. Similarly on the source side,

$$\mathbf{V}(0, s) = \mathbf{Z}_{in}(s)\mathbf{I}(0, s) \quad (3.55)$$

where $\mathbf{Z}_{in}(s)$ is an 8-by-8 unknown matrix. Using Equations 3.53, 3.54 and 3.55, the input impedance matrix to the line elements of the coil, $\mathbf{Z}_{in}(s)$, is calculated as:

$$\mathbf{Z}_{in}(s) = [\mathbf{\Phi}_{11}(s) - \mathbf{Z}_L\mathbf{\Phi}_{21}(s)]^{-1} [\mathbf{Z}_L\mathbf{\Phi}_{22}(s) - \mathbf{\Phi}_{12}(s)] \quad (3.56)$$

The end capacitors on the source side and a 50- Ω Thevenin source are added to the circuit, as shown in Figure 3–7. The source current I_s and the line element currents I_i for $i = 1\dots 8$ are solved using mesh analysis. Figure 3–7 shows the mesh loops using red arrows and indicates the chosen current directions.

The source current I_s provides some insight on the coil's overall response to stimulus. One useful measure is the S_{11} -parameter, which calculates the ratio of

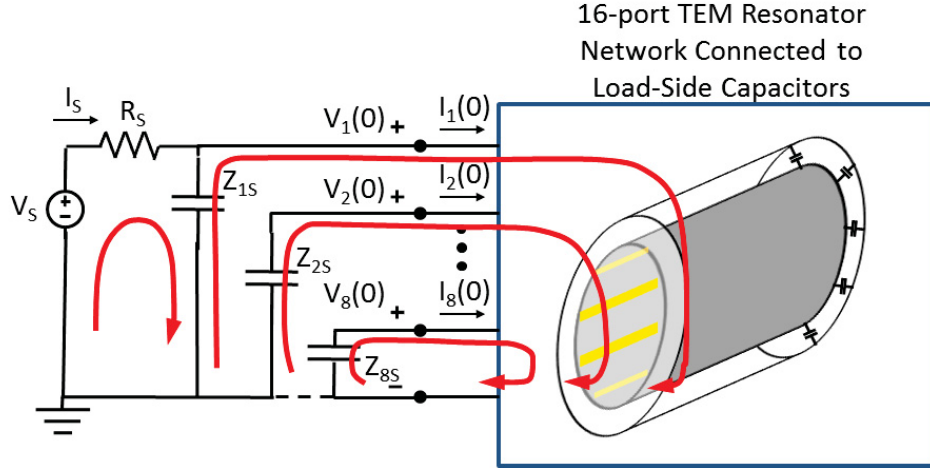


Figure 3-7: The full circuit representation of the TEM resonator driven by a source V_s on the first conductor. The red arrows indicate the direction of the currents used in the mesh analysis.

reflected power over incident power. The S_{11} -parameter is defined as:

$$S_{11} = \frac{Z'_{in} - R_s}{Z'_{in} + R_s} \quad (3.57)$$

where Z'_{in} is the input impedance seen by the source. In the TEM resonator, the input impedance is simply:

$$Z'_{in} = \frac{V_s}{I_s} - R_s \quad (3.58)$$

By calculating I_s over a range of frequencies of interest, the operating frequency corresponding to optimal coil efficiency is found as the smallest $S_{11}(s)$ value.

The line element currents from the mesh analysis carry information about the response to stimulus in different parts of the coil. The voltage boundary conditions at the input of the line elements relate to the line element currents through Equation 3.55. From $\mathbf{V}(0, s)$ and $\mathbf{I}(0, s)$, the voltage and current on every line element can

be calculated at any position along the length of the coil through Equation 3.52. It also follows that the electric and magnetic fields can be determined anywhere within the coil, one transverse slice at a time. In the case of the electric field, the electric potential distribution $V(x, y)$ is obtained by solving Poisson's Equation 3.17 with the boundary conditions prescribed in $\mathbf{V}(z, s)$. Alternatively, $V(x, y)$ can be regarded as a superposition of eight voltage distributions $V_i(x, y)$ where the boundary conditions are $V = V_i(z, s)$ on the i -th conductor and $V = 0$ on all other conductors [20]. This approach avoids computing new solutions to Poisson's equations since the voltage distributions calculated during the PUL parameter step are simply scaled versions of $V_i(x, y)$. Therefore, the voltage distribution at slice z is:

$$V(x, y) = \frac{1}{V_0} \sum_{i=1}^8 V_i(z, s) \tilde{V}_i(x, y) \quad (3.59)$$

where V_0 is the voltage on the i -th conductor during the computation of $\tilde{V}_i(x, y)$. The electric field $\vec{E}(x, y)$ then derives from the electric potential through Equation 3.16. In the case of the magnetic field, the current conditions $\mathbf{I}(z, s)$ are enforced by setting the magnetic potential on each line element according to $\Psi(z, s) = \mathbf{L}\mathbf{I}(z, s)$. Similarly to the electric field approach, the solutions to Poisson's Equation 3.21 computed during the PUL parameter step are superimposed and scaled according to $\Psi(z, s)$:

$$A_z(x, y) = \frac{1}{\psi_0} \sum_{i=1}^8 \psi_i(z, s) \tilde{A}_{z,i}(x, y) \quad (3.60)$$

where ψ_0 is the magnetic potential on the i -th conductor during the computation of $\tilde{A}_{z,i}(x, y)$. The magnetic field $\vec{H}(x, y)$ derives from the magnetic potential through Equation 3.18.

3.3 Three-Dimensional Full-Wave EM Model

Once the TEM resonator design is finalized using the MTL model, the coil must be readjusted to account for the loading effect of the tissue phantom. Three-dimensional full-wave methods are necessary to accurately capture the complex non-TEM effects that occur in realistic transmission lines. There are three major numerical methods in electromagnetics: finite-difference time-domain (FDTD), finite-element method (FEM) and method of moments (MoM). Central to all methods is the discretization of the problem domain into a large number of small elements, over which one unknown electromagnetic quantity (e.g. electric field) is computed. The methods are fundamentally different from one another in their approach to solving Maxwell's equations therefore, their performance in speed and accuracy can vary significantly depending on the problem.

For the purpose of MRI coils, the FDTD method is the most common approach [8]. The MoM is ideal for radiation (far-field) applications or problems composed of perfectly conducting materials; however, the formulation adapts poorly to inhomogeneous dielectric structures, such as tissue models. For a single frequency solution, the speed performance of FEM and FDTD are comparable. Moreover, by virtue of its versatile meshing capabilities, an FEM model will conform more closely to the actual geometries. However during the design of the coil where a spectrum of the solution is desirable, FDTD is the preferred option since it computes a broadband solution at no extra cost. Also, most commercial software packages include extensions to FDTD to improve the geometrical accuracy [21].

The following sections describe the 3D full-wave model of the TEM resonator. Although a thorough discussion of the FDTD method is beyond the scope of this thesis, a brief overview of the theory and the relevant measurements extracted from the 3D model are presented.

3.3.1 FDTD Method

The finite-difference time-domain method is a numerical algorithm that explicitly calculates the electric and magnetic fields using Maxwell's curl equations rather than solving the wave equation, as it is done in FEM and MoM. The cornerstone of FDTD lies in computing \vec{E} and \vec{H} on two distinct Cartesian grids that are staggered in both space and time, a technique proposed by Kane Yee in 1966. The method was validated by Allen Taflove in 1975, when he published the correct criterion for numerical stability [22]. Despite FDTD's straightforward implementation, the technique only started gaining popularity in the 1980s, when the rapidly increasing memory in commercial computers satisfied the large storage needs of FDTD. Today, commercial versions, such as SEMCAD X[®] and CST Microwave Studio[®], include powerful extensions to the standard algorithm and a practical user interface.

Considering a region without electric or magnetic current sources, Faraday's and Ampère's law in point form from Equations 3.10 and 3.11 yield six coupled scalar

equations. In Cartesian coordinates, these equations are:

$$\frac{\partial H_x}{\partial t} = \frac{1}{\mu} \left(\frac{\partial E_y}{\partial z} - \frac{\partial E_z}{\partial y} \right) \quad (3.61a)$$

$$\frac{\partial H_y}{\partial t} = \frac{1}{\mu} \left(\frac{\partial E_z}{\partial x} - \frac{\partial E_x}{\partial z} \right) \quad (3.61b)$$

$$\frac{\partial H_z}{\partial t} = \frac{1}{\mu} \left(\frac{\partial E_x}{\partial y} - \frac{\partial E_y}{\partial x} \right) \quad (3.61c)$$

$$\frac{\partial E_x}{\partial t} = \frac{1}{\varepsilon} \left(\frac{\partial H_y}{\partial z} - \frac{\partial H_z}{\partial y} - \sigma E_x \right) \quad (3.61d)$$

$$\frac{\partial E_y}{\partial t} = \frac{1}{\varepsilon} \left(\frac{\partial H_z}{\partial x} - \frac{\partial H_x}{\partial z} - \sigma E_y \right) \quad (3.61e)$$

$$\frac{\partial E_z}{\partial t} = \frac{1}{\varepsilon} \left(\frac{\partial H_x}{\partial y} - \frac{\partial H_y}{\partial x} - \sigma E_z \right) \quad (3.61f)$$

By discretizing the region of interest into small voxels, the spacial derivatives in Equations 3.61a to 3.61f are approximated by finite differences (FD). We will consider for simplicity a regular Cartesian grid where the dimensions of a single element are Δx , Δy and Δz in the x , y and z coordinate directions, respectively. Moreover, the time derivatives are also expressed as finite differences by sampling \vec{E} and \vec{H} at every time step Δt . As an example, Equations 3.61a and 3.61d at point $(i\Delta x, j\Delta y, k\Delta z, n\Delta t)$ are, in terms of central finite differences:

$$\frac{H_x|_{i,j,k}^{n+1/2} - H_x|_{i,j,k}^{n-1/2}}{\Delta t} = \frac{1}{\mu} \left[\frac{E_y|_{i,j,k+1/2}^n - E_y|_{i,j,k-1/2}^n}{\Delta z} - \frac{E_z|_{i,j+1/2,k}^n - E_z|_{i,j-1/2,k}^n}{\Delta y} \right] \quad (3.62)$$

and

$$\frac{E_x|_{i,j,k}^{n+1/2} - E_x|_{i,j,k}^{n-1/2}}{\Delta t} = \frac{1}{\varepsilon} \left[\frac{H_y|_{i,j,k+1/2}^n - H_y|_{i,j,k-1/2}^n}{\Delta z} - \frac{H_z|_{i,j+1/2,k}^n - H_z|_{i,j-1/2,k}^n}{\Delta y} - \sigma \frac{E_x|_{i,j,k}^{n+1/2} + E_x|_{i,j,k}^{n-1/2}}{2} \right] \quad (3.63)$$

where we have used the notation $F(i\Delta x, j\Delta y, k\Delta z, n\Delta t) = F|_{i,j,k}^n$ and approximated the conduction current $\sigma E_x|_{i,j,k}^n$ as the average between time points $(n - 1/2)$ and $(n + 1/2)$. Assuming that the field values prior time point $t = (n\Delta t + 1/2)$ are known (i.e. all $\vec{E}|_{i,j,k}^m$ and $\vec{H}|_{i,j,k}^m$ for $m \leq n$), $E_x|_{i,j,k}^{n+1/2}$ and $H_x|_{i,j,k}^{n+1/2}$ in Equations 3.62 and 3.63 can be computed *explicitly*. Therefore, \vec{E} and \vec{H} are explicitly computed using a time-stepping method given the initial conditions of the fields, thereby avoiding costly matrix inversions techniques. Although other forms of finite differences exist, the choice in central FD produces a unique arrangement between the \vec{E} and \vec{H} components. As demonstrated in Equations 3.62 and 3.63, the magnetic and electric field samples relate to each other in terms of a time offset of $\Delta t/2$. Moreover, the magnetic field samples depend on four surrounding electric field components located at half a voxel distance away, and vice versa. In this arrangement, the magnetic and electric field samples are computed in staggered locations within each voxel and on interleaved time points. Figure 3-8 illustrates this arrangement commonly referred to as the Yee cell.

Since the inception of FDTD, many refinements and extensions to the method have improved its performance and expanded the range of applications. Although an in-depth understanding of every facet of FDTD would require years of study, many commercial and open source softwares available today make this powerful technique

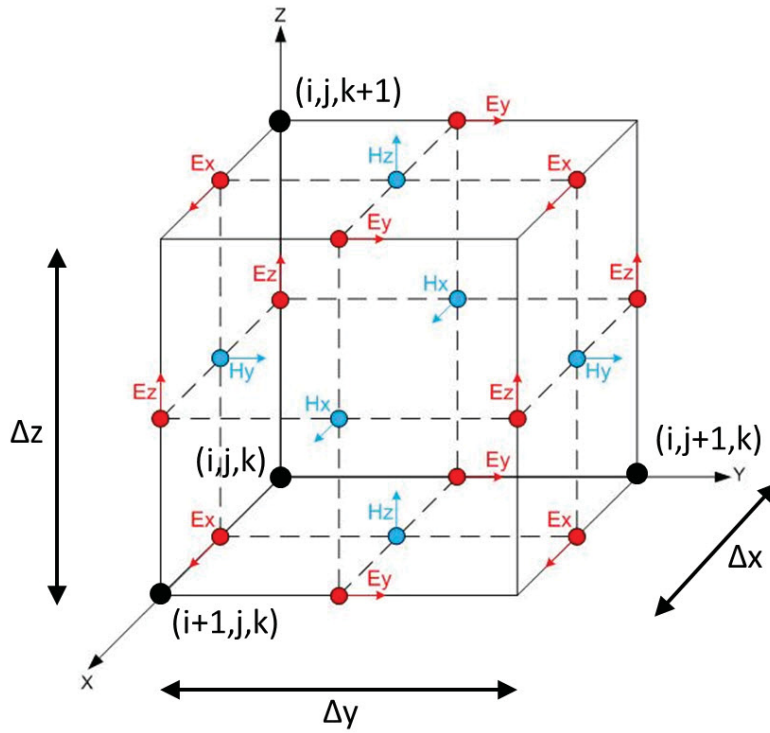


Figure 3–8: The Yee cell (adapted from [2]).

accessible to even the most novice users. The commercial software SEMCAD X[®] developed by Schmid & Partner Engineering (SPEAG) is one of the leading platforms for 3D full wave simulation using FDTD. It was selected to model the TEM resonator for its specialization in medical applications. Following the computation of the electric and magnetic fields through FDTD, the important electrical characteristics of the TEM resonator can be extracted from the results.

CHAPTER 4

Transmit Coil Model Measurements

For the purpose of carrying out a simulation experiment on parallel transmission RF pulses, two RF coil simulation models are generated following the methodology proposed in Chapter 3. The design of a single coil begins with the development of an MTL model tuned to the desired resonance characteristics. Then, using a full-wave FDTD model, the coil is refined to account for non-TEM effects and is adjusted for the loading effects caused by coupling between the coil and the tissues. The following sections present the results from the MTL model and the full-wave FDTD model for an unloaded coil, and compare their agreement to the study conducted by Bogdanov and Ludwig [20]. The final section assesses the loading effects on the coil response and presents the corrected coil designs.

4.1 MTL Model Results

Two TEM resonator models are constructed using the MTL approach: one 128-MHz coil for 3T MRI systems and one 300-MHz coil for 7T MRI systems. The basic design of the TEM resonator is shown in Figures 3-1a and 3-2. By modifying certain features of the coil, such as the geometry and the values of the lumped elements, the electrical characteristics of the coil change. The length of the coil and the radii of the shield and line element cylinders are fixed dimensions in accordance with standard head coils. Therefore, there are three coil parameters that can be adjusted to tune the resonance: the capacitors and the width and thickness of the line elements. For

the sake of design simplicity and optimal B_1^+ uniformity, each parameter is scaled by the same amount on all line elements. By virtue of symmetry, all eight input responses are identical thereby necessitating characterization of only one input of the TEM resonator.

4.1.1 Coil Parameter Characterization

Figure 4–1 shows the S_{11} parameter in decibels of one input to the TEM resonator in the frequency range of interest. The coil response exhibits four resonances: 176, 200, 215 and 222 MHz. In this specific example, the capacitor values are set to 10 pF and the width and thickness of the line elements are set to 24 mm and 35 μm , respectively. In order to understand how to tune the TEM resonator, the parameters are altered one at a time in incremental amounts and their effect measured by the coil response.

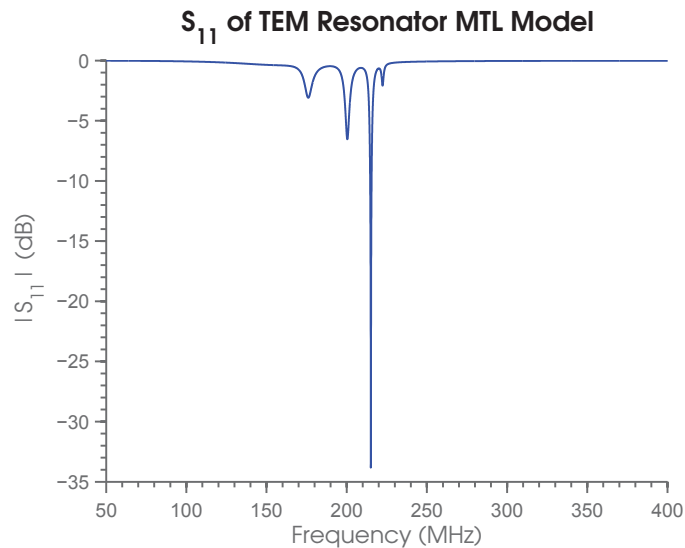


Figure 4–1: The S_{11} spectrum of the TEM resonator predicted by the MTL model, where the capacitor values are set to 10 pF and the width and thickness of the line elements are 24 mm and 35 μm , respectively.

Figure 4–2 shows the S_{11} parameter in decibels for varying line element thicknesses. Since the coil response has multiple resonances located near each other in the frequency spectrum, the portion of the S_{11} curve belonging to the *first* resonance is plotted for each parameter configuration. For every curve, the line element width and capacitances are kept at a constant value of 24 mm and 10 pF, respectively. The results show that an increase in the line element thickness produces a downward shift in the resonant frequency and a slight decrease of the S_{11} at resonance. By doubling the thickness of the line element, a decrease of approximately 1 MHz is observed in the resonant frequency. A similar shift is observed on the portions of the S_{11} curves belonging to the second and third resonances but are not plotted here for brevity.

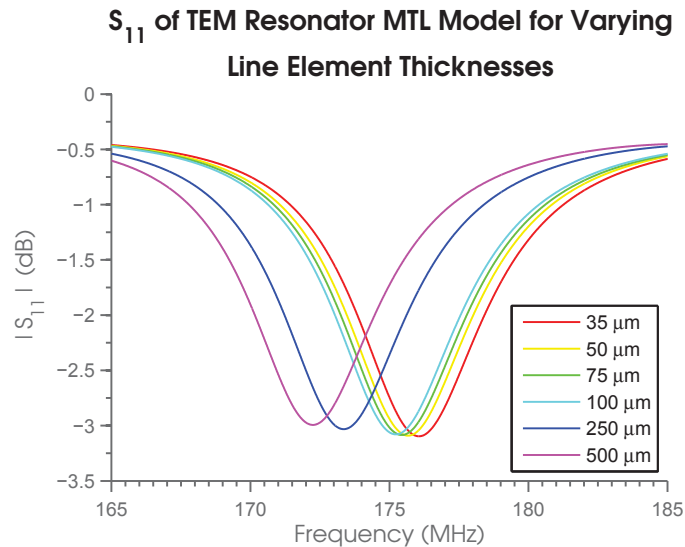


Figure 4–2: The comparison of the S_{11} spectra from the MTL model for varying line element thicknesses. These curves show an upward shift in the resonance for increasing line element thickness.

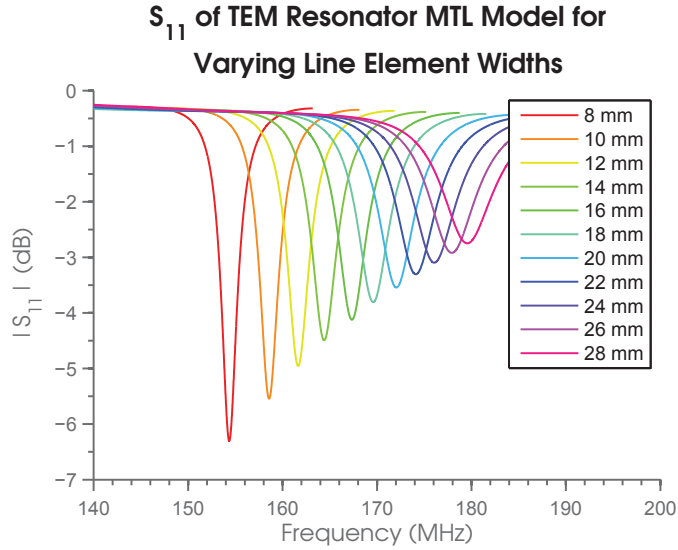


Figure 4–3: The comparison of the S_{11} spectra from the MTL model for varying line element widths. These curves show a downward shift in the resonance for increasing line element width.

Figure 4–3 shows the S_{11} parameter of the first resonance peak for varying line element widths, where the line element thickness and capacitances are kept at a constant value of $35 \mu\text{m}$ and 10 pF , respectively. For an increase in the line element width by a factor of 2, an upward shift of the resonance of 15 MHz and decrease of the S_{11} at resonance are observed.

Finally, the coil response is characterized for different capacitor values. Figure 4–4 shows the S_{11} parameter of the first resonance peak for varying capacitor values, where the line element width and thickness are 24 mm and $35 \mu\text{m}$, respectively. In the frequency spectrum of interest, doubling the capacitor value produces a downward frequency shift of approximately 50 MHz accompanied by a slight variation in the S_{11} at resonance.

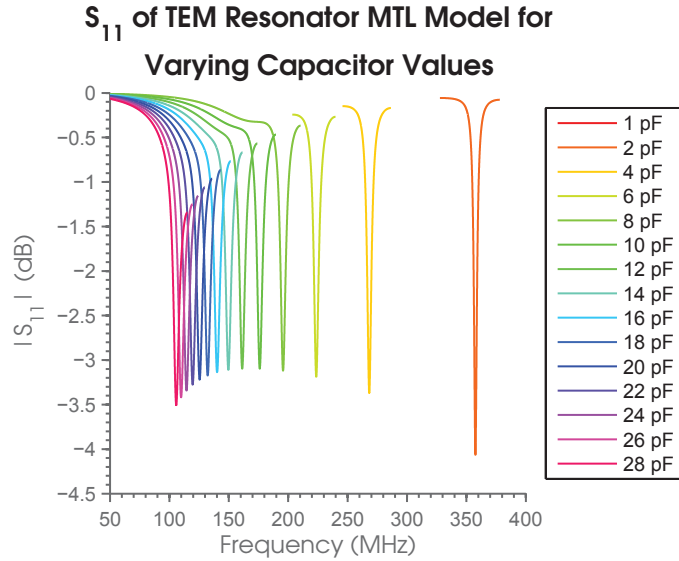


Figure 4–4: The comparison of the S_{11} spectra from the MTL model for varying capacitor values. These curves show an downward shift in the resonance for increasing capacitor values.

4.1.2 Coil Parameter Selection

Using the trends exposed in Figures 4–2 to 4–4, a coil configuration is selected for each desired resonance. The sensitivity of the coil response to the thickness of the line elements is negligible compared to the other two parameters. Therefore for design simplicity, an industry-standard thickness of $35 \mu\text{m}$ is selected for both configurations. Many combinations of line element widths and capacitor values produce the desired resonance frequencies. A preference is given to pairs of combinations that have the same line element width. Maintaining the line element width between models will help in the fabrication stage of the coil. Moreover, line element widths under 30 mm are preferred in order to minimize the patient’s claustrophobic discomfort during scans. The selected parameters are shown in Table 4–1. Figure 4–5 shows

the S_{11} curves of both coils. The electric and magnetic field distributions are also calculated for each coil design. Figures 4–6 and 4–7 show the normalized magnitude of the \vec{E} and \vec{B} fields of the 3T and 7T coil cross-section at $z = L/2$, respectively, where the magnitude of the fields are calculated as:

$$|\vec{F}(\vec{r})| = \sqrt{F_x(\vec{r})^2 + F_y(\vec{r})^2} \quad (4.1)$$

Table 4-1: The TEM resonator parameter settings determined by the MTL model for the 3T (128 MHz) and 7T (300 MHz) coils.

| f_0 (MHz) | Capacitor Value (pF) | Line Element Width (mm) | Line Element Thickness (μm) |
|----------------|-------------------------|----------------------------|---|
| 128 | 18.8 | 22 | 35 |
| 300 | 3 | 22 | 35 |

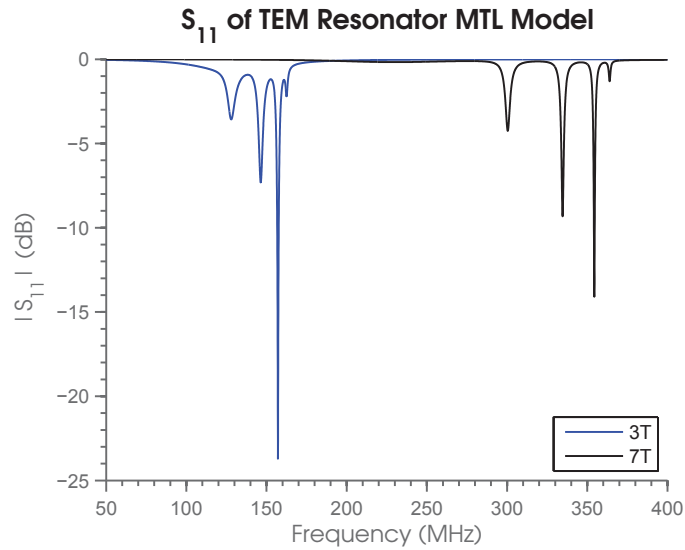


Figure 4-5: The S_{11} spectra of the 3T (128 MHz) and 7T (300 MHz) TEM resonator predicted by the MTL model.

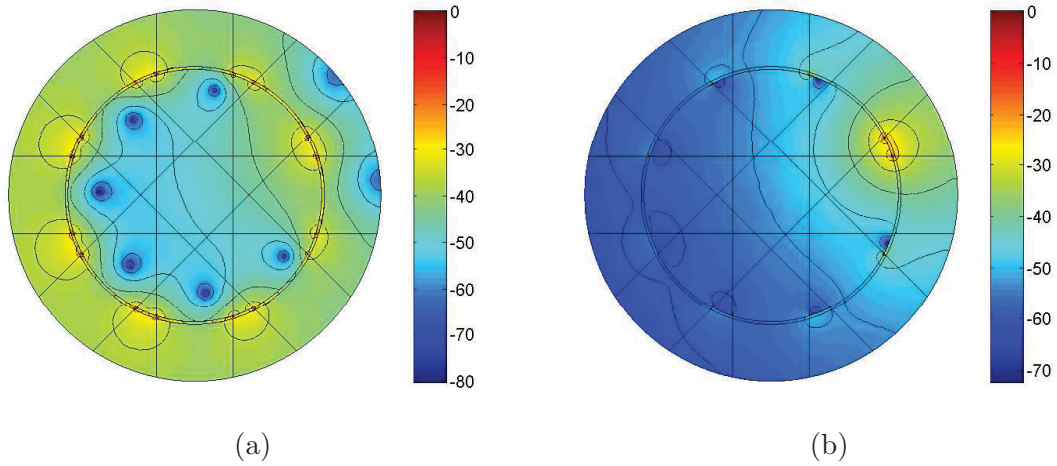


Figure 4–6: The normalized (a) electric and (b) magnetic field magnitude distribution of the 3T (128 MHz) TEM resonator predicted by the MTL model, at the $z = L/2$ cross-section. The two inner circles drawn in black delimit the dielectric subdomain, whereas the intersections of the straight lines and the most inner circle mark the edges of the line elements.

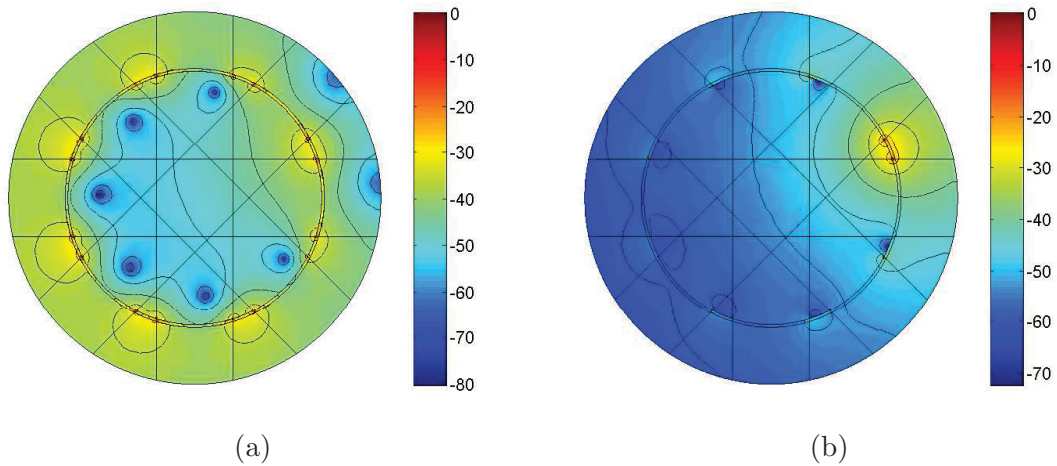


Figure 4–7: The normalized (a) electric and (b) magnetic field magnitude distribution of the 7T (300 MHz) TEM resonator predicted by the MTL model, at the $z = L/2$ cross-section. The two inner circles drawn in black delimit the dielectric subdomain, whereas the intersections of the straight lines and the most inner circle mark the edges of the line elements.

4.2 Full-Wave EM Model Results

A similar exercise as from Section 4.1 is carried out in SEMCAD X[®] on the coil parameters to assess the equivalence between the MTL model and the full-wave EM model. Then, using the parameters from Table 4–1 as starting points, two full-wave EM models are constructed, one for each desired resonant frequency.

4.2.1 Coil Parameter Characterization

Figure 4–8 shows the S_{11} parameter in decibels of one input to the TEM resonator in the frequency range of interest. The coil response exhibits four resonances: 150, 159, 168 and 173 MHz. The design parameters used to generate this result are the same as those from Figure 4–1.

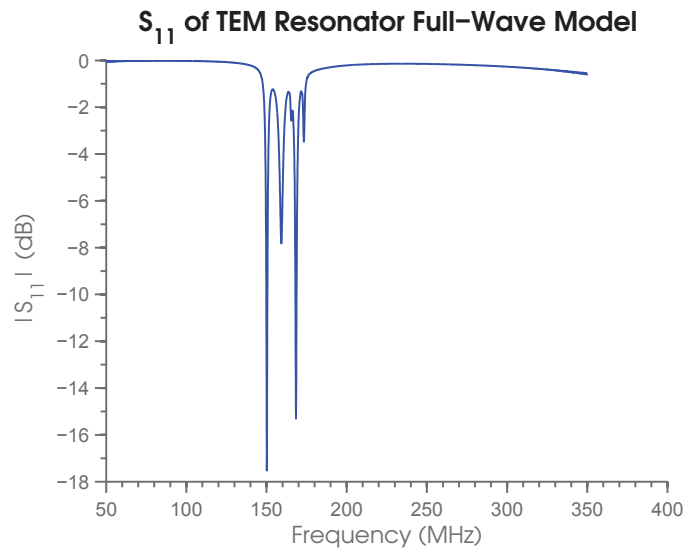


Figure 4–8: The S_{11} spectrum of the TEM resonator predicted by the full-wave EM model, where the capacitor values are set to 10 pF and the width and thickness of the line elements are 24 mm and 35 μm , respectively.

Figure 4–9 shows the S_{11} parameter (in dB) for varying line element thicknesses, where the line element width and capacitor values are 24 mm and 10 pF, respectively. The variation of the line element thickness produces a very negligible effect on the coil response. For an increase in thickness by a factor of 2, the S_{11} curve shifts upwards by less than 100 kHz.

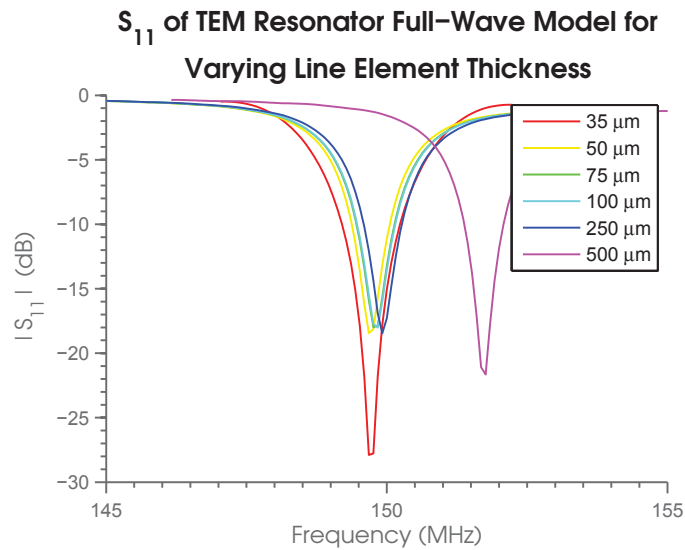


Figure 4–9: The comparison of the S_{11} spectra from the full-wave EM model for varying line element thicknesses. These curves show an upward shift in the resonance for increasing line element thickness.

The effect of varying the line element width is shown in Figure 4–10, where the line element thickness is kept at 35 μm and the capacitors at 10 pF. By doubling the line element width, the S_{11} curve shifts upwards in frequency by approximately 13 MHz. A decrease in the S_{11} value is also observed.

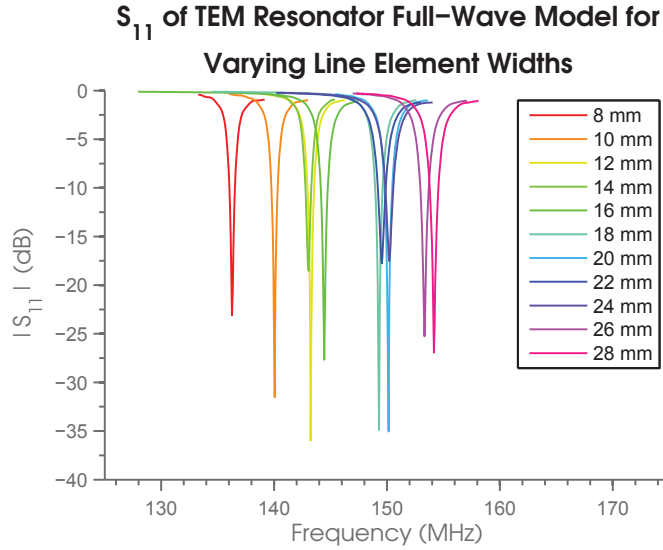


Figure 4–10: The comparison of the S_{11} spectra from the full-wave EM model for varying line element widths. These curves show an upward shift in the resonance for increasing line element widths.

Finally, the full-wave model coil response is characterized for varying capacitor values, where the line element width and thickness are 24 mm and 35 μm , respectively. From Figure 4–11, we observe a downward shift in frequency on the order of 50 MHz for an increase in capacitance by a factor of 2. Moreover, an increase in the S_{11} is observed.

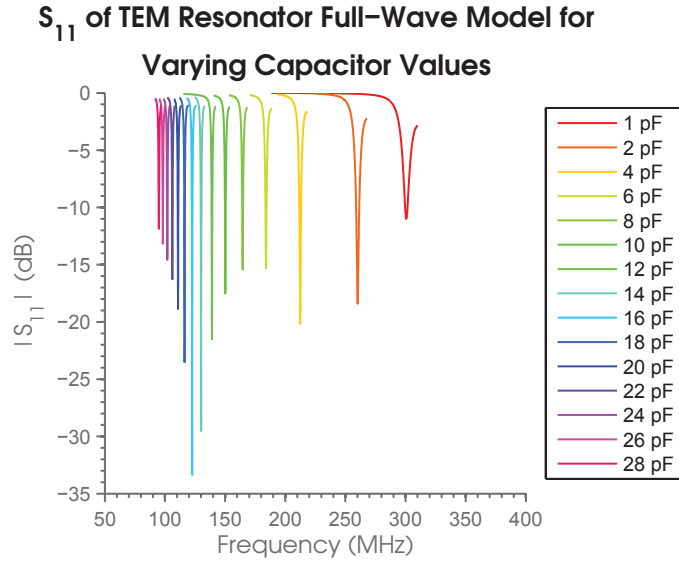


Figure 4-11: The comparison of the S_{11} spectra from the full-wave EM model for varying capacitor values. These curves show a downward shift in the resonance for increasing capacitor values.

4.2.2 Comparison of the MTL Model and the Full-Wave Model

The coil responses measured by the MTL model and the full-wave EM model show some similarities. From Figures 4-1 and 4-8, we observe that both models of the TEM resonator predict four resonances in the frequency spectrum of interest. There are also similarities between the models in terms of the trends observed while varying the design parameters.

Using the results from Figures 4-3 and 4-10, the effects of varying the line element width results are compared in Figure 4-12 in terms of two features: the resonant frequency, f_0 , and the value of the S_{11} at resonance. In Figure 4-12a, we observe an average 15% disparity in the resonant frequency between the two models. The disparity increases monotonically with increasing resonant frequency. Despite

the difference in the absolute values of the resonant frequencies, the progression of the resonance spectrum in both models follow a similar trend. Figure 4–12b compares the S_{11} parameter (in dB) at f_0 for varying line element widths. The MTL model does not accurately predict the S_{11} value in the full-wave EM model, nor is there an observable trend common to both models.

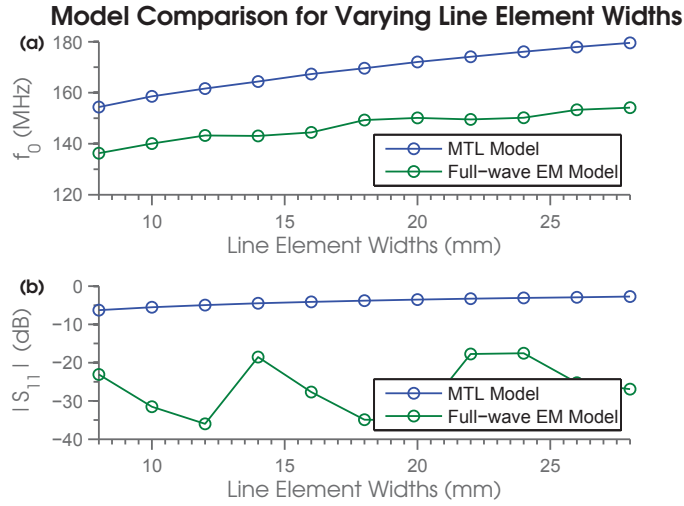


Figure 4–12: The comparison of the (a) resonance frequency, f_0 , and (b) the S_{11} parameter (in dB) calculated by the MTL model and full-wave EM model for varying line element widths.

In a similar manner, Figure 4–13 presents the results from Figures 4–4 and 4–11 in order to compare the effects of varying the capacitor values in each model. In Figure 4–13a, we observe a very similar trend in the resonant frequency between the MTL model prediction and the full-wave EM model calculation. As it was the case for varying the line element width, the MTL model curve is approximately 15% above the full-wave model curve at 150 MHz. This discrepancy increases with resonant frequency, reaching the 40% mark at 300 MHz, the frequency of interest for

7T MRI machines. At the The comparison of S_{11} in Figure 4–13b again shows no correlation between the two models.

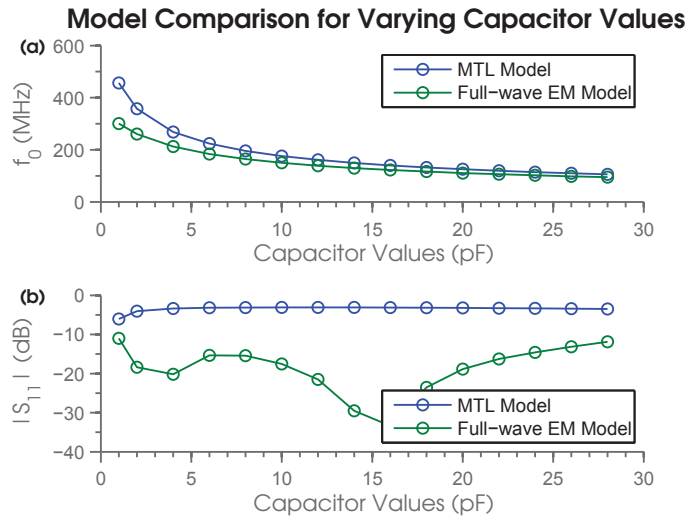


Figure 4–13: The comparison of the (a) resonance frequency, f_0 , and (b) the S_{11} parameter (in dB) calculated by the MTL model and full-wave EM model for varying capacitor values.

The results from Figures 4–2 and 4–9 show that the effect of varying the line element thickness differs between the two methods. This inconsistency is for the most part attributed to the fact that the FDTD algorithm models very thin metallic structures as a 2D plane staircase. As a result of this approximation, the concept of thickness is lost. However, since varying the thickness by a factor of 10 produces a shift in the resonance spectrum of less than 1%, this discrepancy between the two models is negligible.

The experiment conducted by Bogdanov and Ludwig [20] compares the coil response predictions from the MTL model to measurements performed on real TEM resonator coils. Two small animal coils were used, one with a 36.3 mm radius bore

and one with a 61.4 mm radius bore. Using their results, the performance of the human head coil MTL model is evaluated. In terms of the resonant frequency, the MTL models of the animal coils report an error margin of 4% for the smaller coil and 5% for the larger coil around 175 MHz; from Figure 4–13a, the human head coil MTL model has an error margin of 10% around the same frequency. Some amount of inaccuracy is expected since the MTL model does not account for the non-TEM effects occurring in the coil. Moreover, the radius increase from the smaller animal coil to the larger one showed an increase in the percent error. The human head coil has a bore radius of 129.5 mm, which is approximately twice the size of the large animal coil radius. Therefore, the larger discrepancy is attributed to the difference in diameters. In terms of the S_{11} values, the animal coil experiment does not show a strong correlation between the MTL model and the coil measurements. This was also the observation in the human head coil model comparison.

4.2.3 Coil Parameter Selection

Starting from the coil configurations identified by the MTL model, a full-wave EM model is created for each desired frequency. From the comparison study, it is already known that the values from Table 4–1 result in slightly higher than desired resonance spectra. Either decreasing the capacitor values, increasing the line element widths or a combination of both yields the desired effect. By choosing to only tune the capacitor values, the geometry agreement between the MTL and full-wave models is maintained, which simplifies the comparison of the field distributions. Table 4–2 shows the final coil configurations for the full-wave model. Figure 4–14 shows the S_{11} curves of both coils and Figures 4–15 and 4–16 show the normalized magnitude

of the \vec{E} and \vec{B} fields in the 3T and 7T coil cross-section at $z = L/2$. By comparing full-wave model Figures 4–15 and 4–16 and MTL model Figures 4–6 and 4–7, the discrepancy between the two models in predicting the field distributions is more pronounced in the 7T coil than in the 3T coil, a result that is consistent with the comparison of the S_{11} curves.

Table 4–2: The TEM resonator parameter settings determined by the full-wave model for the 3T (128 MHz) and 7T (300 MHz) coils.

| f_0 (MHz) | Capacitor Value (pF) | Line Element Width (mm) | Line Element Thickness (μm) |
|----------------|-------------------------|----------------------------|---|
| 128 | 14.1 | 22 | 35 |
| 300 | 1.3 | 22 | 35 |

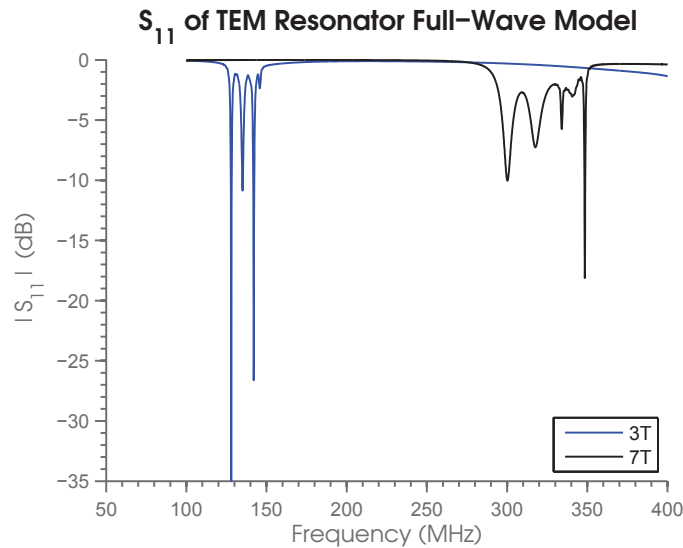
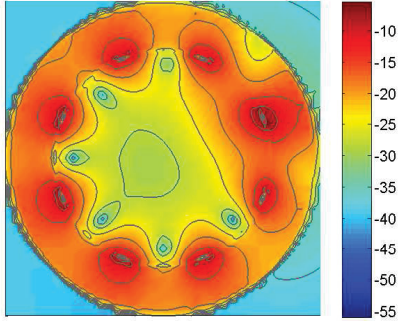


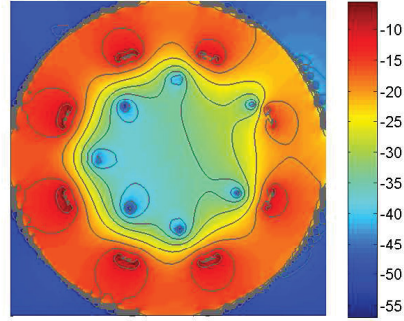
Figure 4–14: The S_{11} spectra of the 3T (128 MHz) and 7T (300 MHz) resonator predicted by the full-wave EM model.

$|E_{xy}|$ (dB) of 3T TEM Resonator



(a)

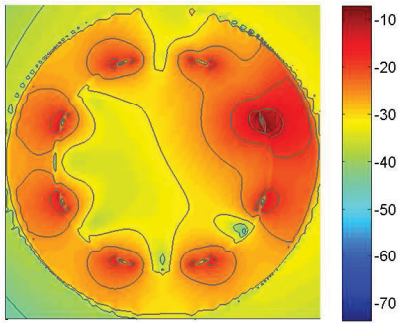
$|B_{xy}|$ (dB) of 3T TEM Resonator



(b)

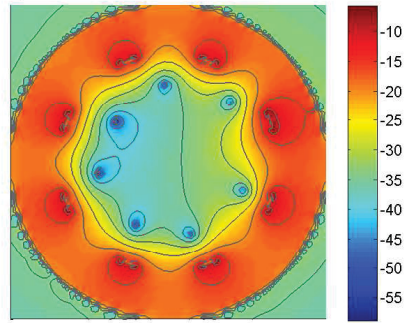
Figure 4–15: The normalized (a) electric and (b) magnetic field magnitude distribution of the 3T (128 MHz) TEM resonator predicted by the full-wave model, at the $z = L/2$ cross-section.

$|E_{xy}|$ (dB) of 7T TEM Resonator



(a)

$|B_{xy}|$ (dB) of 7T TEM Resonator



(b)

Figure 4–16: The normalized (a) electric and (b) magnetic field magnitude distribution of the 7T (300 MHz) TEM resonator predicted by the full-wave model, at the $z = L/2$ cross-section.

4.3 Loaded Coil Adjustments

As the final design step, the coil response is measured under loaded conditions by inserting a phantom into the full-wave coil model. The coil parameters are then adjusted to regain resonance at the correct frequencies.

The phantom design follows the methodology proposed in [3]. A cylindrical phantom of 120 mm in radius, consisting of a uniform dielectric material is inserted coaxially into the coil model. The electromagnetic properties of the material are selected to match the average properties of the human head, as determined by [1]. Table 4–3 lists these properties for 128 and 300 MHz.

Table 4–3: The electromagnetic properties of the human head phantom as calculated by [1].

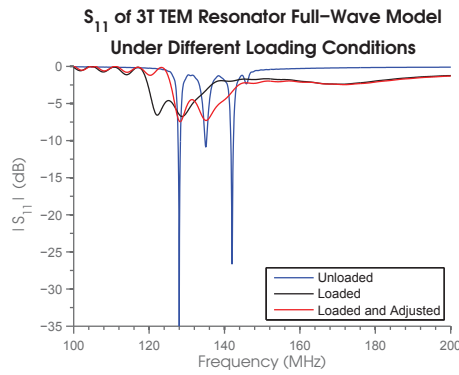
| f_0 (MHz) | Relative Permittivity | Relative Permeability | Electrical Conductivity (S/m) |
|----------------|--------------------------|--------------------------|----------------------------------|
| 128 | 63.1 | 1 | 0.46 |
| 300 | 52 | 1 | 0.55 |

Figures 4–17a and 4–17b compare the S_{11} curves under different conditions, for the 3T and 7T coils, respectively. The blue line corresponds to the response of the unloaded coil; the black line describes the response of the coil containing the phantom. In both the blue and black line responses, the unadjusted coil designs from Table 4–2 were used. By adjusting the capacitor values on the 3T and 7T coils, the coil resonances are shifted back to the correct frequencies. The red lines in Figure 4–17 show the responses of the adjusted 3T and 7T coils, where the design parameters used are those from Table 4–4. The field distributions in Figures 4–18 and 4–19 show

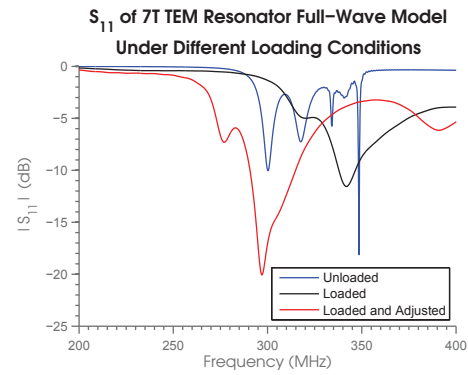
the normalized magnitude of the \vec{E} and \vec{B} fields in the coil cross-section at $z = L/2$ for the adjusted 3T and 7T coils, respectively.

Table 4–4: The TEM resonator parameter settings determined by the full-wave EM model for the 3T (128 MHz) and 7T (300 MHz) coils, adjusted for the loading effects.

| f_0 (MHz) | Capacitor Value (pF) | Line Element Width (mm) | Line Element Thickness (μm) |
|----------------|-------------------------|----------------------------|---|
| 128 | 12.7 | 22 | 35 |
| 300 | 2 | 22 | 35 |



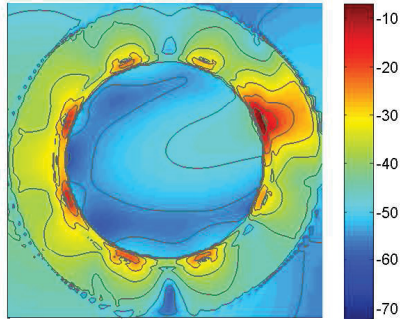
(a) 3T TEM Resonator.



(b) 7T TEM Resonator.

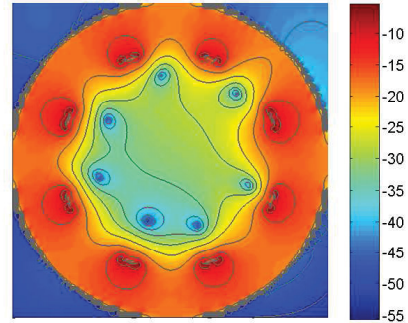
Figure 4–17: The comparison of the S_{11} spectra of the unloaded (blue); loaded (black); and loaded and adjusted (red) TEM resonators predicted by the full-wave EM model.

$|E_{xy}|$ (dB) of 3T TEM Resonator



(a)

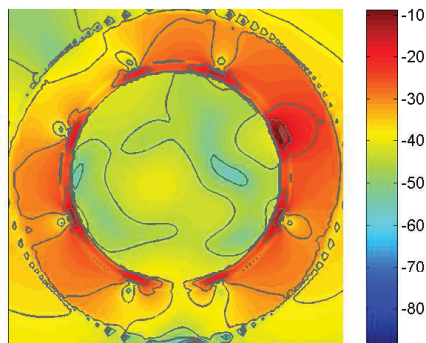
$|B_{xy}|$ (dB) of 3T TEM Resonator



(b)

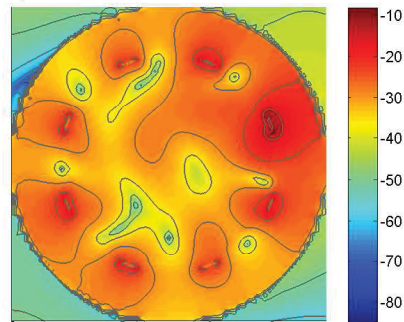
Figure 4-18: The normalized (a) electric and (b) magnetic field magnitude distribution of the loaded and adjusted 3T (128 MHz) TEM resonator predicted by the full-wave model, at the $z = L/2$ cross-section.

$|E_{xy}|$ (dB) of 7T TEM Resonator



(a)

$|B_{xy}|$ (dB) of 7T TEM Resonator



(b)

Figure 4-19: The normalized (a) electric and (b) magnetic field magnitude distribution of the loaded and adjusted 7T (300 MHz) TEM resonator predicted by the full-wave model, at the $z = L/2$ cross-section.

CHAPTER 5

Conclusion

5.1 Summary

A comparative study was performed between two RF coil modelling methods in the context of designing a TEM resonator for high-field MRI applications. The first method is based on the multi-conductor transmission model (MTL), where all wave propagations are assumed to be of transverse electromagnetic (TEM) kind. The second method solves for all types of wave propagation through the computational algorithm called finite-difference time-domain, which yields a more exact solution to the expense of increased computation time. The two methods are compared in terms of the trends observed in the coil response while varying three TEM resonator design parameters: the end-capacitor values, the line element width and line element thickness.

The experiment results show that variations of the end-capacitor values and line element widths in the MTL model and the full-wave model lead to similar trends in the S_{11} spectra. In both models, an increase of the capacitance causes a downward shift of the S_{11} curve, whereas as an increase in the line element widths causes an upward shift of the S_{11} . The variation in thickness of the line elements produces a minute shift of the S_{11} curve in both models therefore, it is concluded that the line element thickness does not contribute significantly to the design of the coil.

The MTL model predictions of the resonant frequency are within a 15% agreement of the full-wave model calculations for standard MRI system coils however this error increases with frequency. At 400 MHz, an important operating frequency belonging to high-field MRI applications, the disparity between the models reaches the 40% mark. Although the MTL model predictions are inaccurate, understanding the relationship between the MTL model and the full-wave model provides valuable insight on how to efficiently design TEM resonators for standard and high-field MRI systems. The following summarizes the design strategy. Firstly, the coil response trends are characterized in the MTL model for variations of the important coil design parameters. A configuration of the design parameters is then selected to produce a TEM resonator MTL model with the desired resonance characteristics. Using the MTL model configuration as the starting point and the trends identified in the characterization step as a guide, the coil design is refined in the full-wave model. Finally, the full-wave model is adjusted for the loading effects caused by the neighbouring tissues. This strategy was demonstrated throughout Chapter 4 using as examples the design of a 3T (128 MHz) TEM resonator and a 7T (300 MHz) TEM resonator.

5.2 Future Work

With the help of new modelling techniques, we hope to accelerate the design of RF coils such that a greater portion of the research effort can be dedicated to the real challenges of high-field MRI, such as improving B_1^+ homogeneity and reducing the risk of RF-induced tissue heating. The conclusions from the present study build upon current strategies to provide the reader with an improved methodology for the design of high-field head coils. Small variations in geometry have negligible effect

on the performance of the MTL model however, it should not be blindly extended to the design of significantly larger TEM resonators such as body coils. Further investigation is required to determine the validity of the MTL model in these conditions. In cases where the MTL model deviates too much from the full-wave model, a single-element coil as illustrated in Figure 3-1c could be used as a reduced full-wave model instead of the MTL model. Some studies have reported an interesting aspect of the TEM resonator where the response of the coil relates directly to the response of the single-element building block.

APPENDIX A

Transmission Line Theory

Transmission line theory is based on the fundamental assumption that the fields surrounding conductors propagate in the transverse electromagnetic (TEM) mode. The TEM mode simply guarantees that the electric and magnetic field components in the direction of propagation are zero. The direction of propagation is conventionally assigned to the z -axis, and the transverse components to the xy -plane.

Maxwell's equations in the integral form are:

$$\text{Faraday's Law of Induction: } \oint_{\partial S} \vec{E} \cdot d\vec{l} = -\mu \frac{d}{dt} \iint_S \vec{H} \cdot d\vec{S} \quad (\text{A.1})$$

$$\text{Ampère's Circuital Law: } \oint_{\partial S} \vec{H} \cdot d\vec{l} = \left(\sigma \iint_S + \varepsilon \frac{d}{dt} \right) \vec{E} \cdot d\vec{S} + \iint_S \vec{J}_i \cdot d\vec{S} \quad (\text{A.2})$$

$$\text{Gauss's Law: } \oiint_S \vec{D} \cdot d\vec{S} = Q_{enc} \quad (\text{A.3})$$

$$\text{Gauss's Law for Magnetism: } \oiint_S \vec{B} \cdot d\vec{S} = 0 \quad (\text{A.4})$$

where \vec{E} , \vec{D} , \vec{H} and \vec{B} are the electric field intensity, electric flux density, magnetic field intensity and magnetic flux density, respectively; μ , σ and ε are the medium's magnetic permeability, conductivity and permittivity, respectively; Q_{enc} is the charge enclosed within the surface and \vec{J}_i is the current density impressed on the circuit from an external current source. If the surface S and, by extension, its contour ∂S are chosen to lie in the transverse plane, the surface integral in Equation A.1 must equal zero since the elementary surface vector $d\vec{S}$ is z -directed and $H_z = 0$. Similarly, the

surface integrals of \vec{E} in Equation A.2 are also zero since $E_z = 0$. Hence, in the cross-sectional plane of any transmission line, Equations A.1 and A.2 always satisfy:

$$\oint_{\partial S} \vec{E} \cdot d\vec{l} = 0 \quad (\text{A.5a})$$

$$\oint_{\partial S} \vec{H} \cdot d\vec{l} = \iint_S \vec{J}_i \cdot d\vec{S} \quad (\text{A.5b})$$

Equations A.5a and A.5b are identical to those for electrostatics therefore, voltage and current are uniquely defined in the transverse plane as:

$$V(z, t) = \int_{c'} \vec{E} \cdot d\vec{l} \quad (\text{A.6a})$$

$$I(z, t) = \oint_c \vec{H} \cdot d\vec{l} \quad (\text{A.6b})$$

where c' and c are paths defined in the transverse plane at position z . It is from these results that Maxwell's full-wave three-dimensional equations can be simplified to a pair of one-dimensional circuit theory equations called the transmission line equations. The important equation manipulations are described in the following sections however, a more thorough exposition of transmission line theory can be found in many reference books such as [23].

A.1 Current Equation

The law of conservation of charge — or equivalently, the continuity equation — states that the total current flowing out of any closed surface S must be equal to the decreasing time rate of charge Q_{enc} enclosed by the surface:

$$I_{Total} = \iint_S \vec{J} \cdot d\vec{S} = -\frac{d}{dt} Q_{enc} \quad (\text{A.7})$$

where \vec{J} is the current density. Consider placing a closed, cylindrical surface S over a section of length Δz of one conductor of a multi-conductor transmission line (MTL), as shown in Figure A-1. The surface is chosen to be uniform along the direction of propagation. A z -directed current density $J_i(z)$, originating from some external current generator connected at either end of the conductor, flows through the small Δz section: a current $I(z)$ flows into the end cap surface at position z and $I(z + \Delta z)$ flows out of the end cap surface at position $z + \Delta z$. Conduction currents caused by the electric field in the lossy dielectric also flow through the small surface. Since $E_z = 0$ under the TEM regime, only transverse currents can exist and these currents flow strictly through the sides of the surface. Using Gauss's law to express Q_{enc} in terms of \vec{E} , Equation A.7 becomes:

$$I(z + \Delta z) - I(z) + \sigma \iint_{S_c} \vec{E} \cdot d\vec{S} = -\frac{d}{dt} \varepsilon \iint_{S_c} \vec{E} \cdot d\vec{S} \quad (\text{A.8})$$

where S_c is the surface S without the end caps.

The oriented surface S_c can be defined in terms of a parametrized position vector:

$$\vec{r}(u, v) = x(u, v)\hat{i} + y(u, v)\hat{j} + z(u, v)\hat{k} \quad (\text{A.9})$$

where u and v are the parametric variables defined over some domain. Since the transverse cross-section of the surface is the same regardless of the chosen position z , the z coordinate is fully defined as $z = v$. The domain of v is $D(v) = [z, z + \Delta]$. The coordinates x and y describe the closed contour of the surface in the xy -plane therefore, the domain of u will depend on the parametric equation chosen for the path. The surface integral of the electric field over S_c is parametrized in terms of u

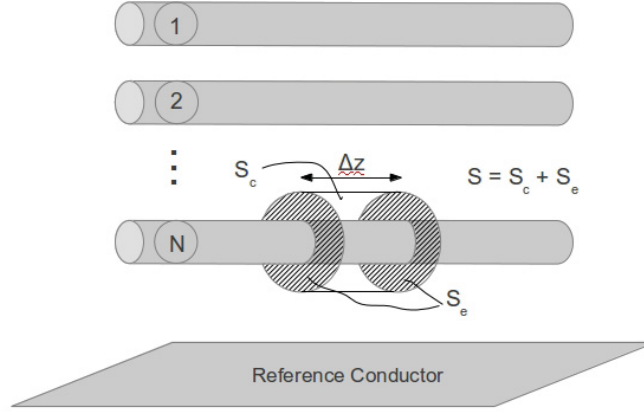


Figure A-1: A multi-conductor transmission line of N conductors where a cylindrical surface S of length Δz was placed around one of the conductors.

and v as follows:

$$\iint_{S_c} \vec{E} \cdot d\vec{S} = \int_z^{z+\Delta z} \int_{u_1}^{u_2} \vec{E}(x(u, v), y(u, v), z(u, v)) \cdot d\vec{S} \quad (\text{A.10})$$

where the elementary vector surface is:

$$d\vec{S} = \hat{n} dS = \frac{d\vec{r}}{du} \times \frac{d\vec{r}}{dv} du dv \quad (\text{A.11})$$

$$= \hat{n} d\vec{l} dv \quad (\text{A.12})$$

Dividing a parametrized version of Equation A.8 by Δz and taking the limit as $\Delta z \rightarrow 0$, as follows:

$$\begin{aligned} \lim_{\Delta z \rightarrow 0} \frac{I(z + \Delta z) - I(z)}{\Delta z} &= -\sigma \lim_{\Delta z \rightarrow 0} \frac{1}{\Delta z} \int_z^{z+\Delta z} \oint_c \vec{E} \cdot \hat{n} \, d\vec{l} \, dv \\ &\quad - \varepsilon \frac{d}{dt} \lim_{\Delta z \rightarrow 0} \frac{1}{\Delta z} \int_z^{z+\Delta z} \oint_c \vec{E} \cdot \hat{n} \, d\vec{l} \, dv \end{aligned} \quad (\text{A.13})$$

leads to the *per-unit-length* continuity equation around the conductor:

$$\frac{\partial I(z)}{\partial z} = -\sigma \oint_c \vec{E} \cdot \hat{n} \, dl - \frac{d}{dt} \varepsilon \oint_c \vec{E} \cdot \hat{n} \, dl \quad (\text{A.14})$$

A.1.0.1 PUL Conductance

The transverse electric field surrounding the conductor is a result of potential differences between itself and its neighbouring conductors. The total conduction current can be separated into current contributions flowing to or from each neighbour. For example, the per-unit-length (PUL) continuity equation around the i -th conductor in a MTL is:

$$\begin{aligned} \frac{\partial I_i(z)}{\partial z} &= -\sigma \left[\oint_c \vec{E}_{i1} \cdot \hat{n} \, dl + \cdots + \oint_c \vec{E}_{ii} \cdot \hat{n} \, dl + \cdots + \oint_c \vec{E}_{iN} \cdot \hat{n} \, dl \right] \\ &\quad - \varepsilon \frac{d}{dt} \oint_c \vec{E} \cdot \hat{n} \, dl \end{aligned} \quad (\text{A.15})$$

where $I_i(z)$ is the current on the i -th conductor with respect to z ; \vec{E}_{ij} is the electric field resulting from a potential difference between conductors i and j when $i \neq j$, and \vec{E}_{ii} is the electric field resulting from a potential difference between conductor i

and the reference conductor; and $N + 1$ is the number of conductors including the reference conductor.

By definition, conductance is the ratio of the current flowing between two conductors and the voltage separating them:

$$G = \frac{\sigma \iint_S \vec{E} \cdot d\vec{S}}{V(z, t)} \quad (\text{A.16})$$

where $V(z, t)$ is the voltage with respect to z and time and is defined as:

$$V(z, t) = - \int_{c'} \vec{E} \cdot d\vec{l} \quad (\text{A.17})$$

The *per-unit-length* conductance is:

$$g = \lim_{\Delta z \rightarrow 0} \frac{G}{\Delta z} = \frac{\sigma}{V(z, t)} \lim_{\Delta z \rightarrow 0} \frac{\int_z^{z+\Delta z} \oint_c \vec{E} \cdot d\vec{S}}{\Delta z} = \sigma \frac{\oint_c \vec{E} \cdot \hat{n} dl}{- \int_{c'} \vec{E} \cdot d\vec{l}} \quad (\text{A.18})$$

By combining Equations A.18 and A.15, the PUL continuity equation around the i -th conductor can be expressed in terms of the conductance characteristics of the transmission line:

$$\begin{aligned} \frac{\partial I_i(z)}{\partial z} = & - [g_{i1} V_{i1}(z, t) + \cdots + g_{ii} V_{ii}(z, t) + \cdots + g_{iN} V_{iN}(z, t)] \\ & - \epsilon \frac{d}{dt} \oint_c \vec{E} \cdot \hat{n} dl \end{aligned} \quad (\text{A.19})$$

where g_{ij} and V_{ij} are the PUL conductance and voltage between conductors i and j , respectively, when $i \neq j$, and g_{ii} and V_{ii} are the PUL conductance and voltage between conductor i and the reference conductor.

A.1.0.2 PUL Capacitance

Additional to conduction currents are the displacement currents caused by time varying electric fields in the dielectric. These currents are dependent on the permittivity of the medium and the potential differences between conductors. Similar to the exercise carried out on the conduction currents, the displacement currents of the continuity equation are separated into individual current contributions from each neighbouring conductor:

$$\begin{aligned} \frac{\partial I_i(z)}{\partial z} = & -\varepsilon \frac{d}{dt} \left[\oint_c \vec{E}_{i1} \cdot \hat{n} dl + \dots + \oint_c \vec{E}_{ii} \cdot \hat{n} dl + \dots + \oint_c \vec{E}_{iN} \cdot \hat{n} dl \right] \\ & - \sigma \oint_c \vec{E} \cdot \hat{n} dl \end{aligned} \quad (\text{A.20})$$

Capacitance describes the ability of an object to store an electrical charge. It is defined as the ratio of the charge on two conductors, Q_c and $-Q_c$, and the voltage separating them:

$$C = \frac{Q_c}{V(z, t)} = \frac{\varepsilon \iint_S \vec{E} \cdot d\vec{S}}{V(z, t)} \quad (\text{A.21})$$

where Gauss' law was used to replace Q_c . Similar to conductance, the *per-unit-length* capacitance is:

$$c = \lim_{\Delta z \rightarrow 0} \frac{C}{\Delta z} = \varepsilon \frac{\oint_c \vec{E} \cdot \hat{n} dl}{-\int_{c'} \vec{E} \cdot d\vec{l}} \quad (\text{A.22})$$

By combining Equations A.22 and A.20, the PUL continuity equation around the i -th conductor can be expressed in terms of the capacitance characteristics of the

transmission line:

$$\begin{aligned} \frac{\partial I_i(z)}{\partial z} = & -\frac{d}{dt} [c_{i1}V_{i1}(z, t) + \cdots + c_{ii}V_{ii}(z, t) + \cdots + c_{iN}V_{iN}(z, t)] \\ & - \sigma \oint_c \vec{E} \cdot \hat{n} dl \end{aligned} \quad (\text{A.23})$$

where c_{ij} and V_{ij} are the PUL capacitance and voltage between conductors i and j , respectively, when $i \neq j$, and c_{ii} and V_{ii} are the PUL capacitance and voltage between conductor i and the shield.

A.2 Voltage Equation

Another useful PUL equation derives from Equation A.1, Faraday's law of induction. Consider placing an open, oriented surface between one conductor of the MTL and the reference conductor, as shown in Figure A-2. The surface is of length Δz and is uniform with respect to the direction of propagation. Integrating along the contour gives:

$$\int_a^{a'} \vec{E}_z \cdot d\vec{l} + \int_{a'}^{b'} \vec{E}_t \cdot d\vec{l} + \int_{b'}^b \vec{E}_z \cdot d\vec{l} + \int_b^a \vec{E}_t \cdot d\vec{l} = -\mu \frac{d}{dt} \iint_S \vec{H} \cdot d\vec{S} \quad (\text{A.24})$$

Since $\vec{E}_z = 0$, the line integrals of \vec{E} along the conductor segments are zero. The line integrals on the transverse plane segments correspond to the voltages between the two conductor at two different positions z :

$$V(z, t) = \int_a^b \vec{E} \cdot d\vec{l} \quad (\text{A.25a})$$

$$V(z + \Delta z, t) = \int_{a'}^{b'} \vec{E} \cdot d\vec{l} \quad (\text{A.25b})$$

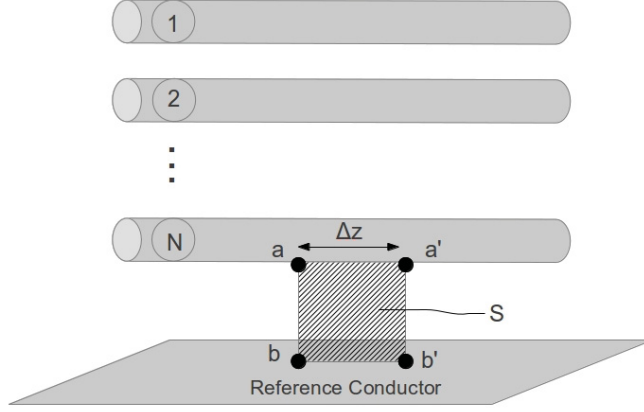


Figure A-2: A multi-conductor transmission line of N conductors where an open surface S of length Δz was placed between one conductor and the reference conductor.

The surface integral over the magnetic field intensity is parametrized in a similar manner as Equation A.10. Combining Equations A.25a and A.25b into a parametrized version of A.24 gives:

$$V(z + \Delta z, t) - V(z, t) = -\mu \frac{d}{dt} \int_z^{z+\Delta z} \int_c \vec{H} \cdot \hat{n} d\vec{l} dv \quad (\text{A.26})$$

where c is the path along the surface S from a to b in the transverse plane. Dividing Equation A.26 by Δz and taking the limit as $\Delta z \rightarrow 0$, as follows:

$$\lim_{\Delta z \rightarrow 0} \frac{V(z + \Delta z) - V(z)}{\Delta z} = \mu \frac{d}{dt} \lim_{\Delta z \rightarrow 0} \frac{1}{\Delta z} \int_z^{z+\Delta z} \int_c \vec{H} \cdot \hat{n} d\vec{l} dv \quad (\text{A.27})$$

leads to the *per-unit-length* induction equation between the conductor of the transmission line and the reference conductor:

$$\frac{\partial V(z)}{\partial z} = \mu \frac{d}{dt} \int_c \vec{H} \cdot \hat{n} dl \quad (\text{A.28})$$

A.2.0.3 PUL Inductance

Faraday's PUL induction equation describes the induced voltage on a conductor by the time varying magnetic field emanating from neighbouring conductors. Similarly to the PUL continuity equation, the total induced voltage can be separated into individual voltage contributions from each neighbouring conductor:

$$\frac{\partial V_i(z)}{\partial z} = \mu \frac{d}{dt} \left[\int_{c'} \vec{H}_{i1} \cdot \hat{n} dl + \dots + \int_{c'} \vec{H}_{ii} \cdot \hat{n} dl + \dots + \int_{c'} \vec{H}_{iN} \cdot \hat{n} dl \right] \quad (\text{A.29})$$

where $V_i(z)$ is the voltage on the i -th conductor with respect to the reference conductor at position z , \vec{H}_{ij} is the magnetic field intensity resulting from current carried on conductors i and j when $i \neq j$, and \vec{H}_{ii} is the magnetic field intensity resulting from a current carried on conductor i and the reference conductor.

Mutual inductance is the ability of a conductor carrying a time-varying current to induce a voltage on neighbouring conductors. It relates the magnetic flux Φ penetrating the surface area between two conductors and the current producing this flux:

$$L = \frac{\Phi}{I(z, t)} = \frac{\mu \iint_S \vec{H} \cdot d\vec{S}}{\oint_c \vec{H} \cdot d\vec{l}} \quad (\text{A.30})$$

where Equation A.6b was used to replace the current. The PUL inductance is:

$$l = \lim_{\Delta z \rightarrow 0} \frac{L}{\Delta z} = \mu \frac{\int \vec{H} \cdot \hat{n} dl}{\oint_c \vec{H} \cdot d\vec{l}} \quad (\text{A.31})$$

By combining Equations A.31 and A.29, the PUL induction equation between the i -th conductor and the neighbouring conductors can be expressed in terms of the inductance characteristics of the transmission line:

$$\frac{\partial V_i(z)}{\partial z} = -\frac{d}{dt} [l_{i1}I_{i1}(z, t) + \cdots + l_{ii}I_{ii}(z, t) + \cdots + l_{iN}I_{iN}(z, t)] \quad (\text{A.32})$$

where l_{ij} and I_{ij} are the PUL inductance and current coupling conductors i and j , respectively, when $i \neq j$; and l_{ii} and I_{ii} are the PUL inductance and current coupling conductor i and the reference conductor.

In summary, Maxwell's four three-dimensional electromagnetic equations simplify to two partial differential equations (PDEs) for each conductor. Around the i -th conductor of a N-conductor transmission line, the continuity and induction equations are:

$$\begin{aligned} \frac{\partial I_i(z, t)}{\partial z} = & - [g_{i1}V_{i1}(z, t) + \cdots + g_{ii}V_{ii}(z, t) + \cdots + g_{iN}V_{iN}(z, t)] \\ & - \frac{d}{dt} [c_{i1}V_{i1}(z, t) + \cdots + c_{ii}V_{ii}(z, t) + \cdots + c_{iN}V_{iN}(z, t)] \end{aligned} \quad (\text{A.33})$$

$$\frac{\partial V_i(z, t)}{\partial z} = -\frac{d}{dt} [l_{i1}I_{i1}(z, t) + \cdots + l_{ii}I_{ii}(z, t) + \cdots + l_{iN}I_{iN}(z, t)] \quad (\text{A.34})$$

Note that the voltages V_{ij} in Equation A.33 are expressed as potential differences between the conductors i and j whereas in Equation A.34, the conductor voltage V_i is always relative to the reference conductor. Rearranging Equation A.33 in terms of voltages relative to the reference conductor gives:

$$\begin{aligned} \frac{\partial I_i(z, t)}{\partial z} = & - \left[-g_{i1}V_1(z, t) + \cdots + \sum_{k=1}^N g_{1k}V_i(z, t) + \cdots - g_{iN}V_N(z, t) \right] \\ & - \frac{d}{dt} \left[-c_{i1}V_1(z, t) + \cdots + \sum_{k=1}^N c_{1k}V_i(z, t) + \cdots - c_{iN}V_N(z, t) \right] \end{aligned} \quad (\text{A.35})$$

For the simple case where $N = 1$, one transmission line and the reference conductor, the transmission line equations are:

$$\begin{cases} \frac{\partial I(z, t)}{\partial z} = -(g + sc)V(z, t) \\ \frac{\partial V(z, t)}{\partial z} = -sLI(z, t) \end{cases} \quad (\text{A.36})$$

where the time derivative $\frac{d}{dt}$ was replaced by the complex Laplace argument s . For N larger than 1, the system of transmission line equations is more easily expressed in matrix form:

$$\begin{cases} \frac{\partial \mathbf{I}(z, t)}{\partial z} = -(G + sC)\mathbf{V}(z, t) \\ \frac{\partial \mathbf{V}(z, t)}{\partial z} = -sL\mathbf{I}(z, t) \end{cases} \quad (\text{A.37})$$

where

$$G = \begin{bmatrix} \sum_{k=1}^N g_{1k} & -g_{12} & \cdots & -g_{1N} \\ -g_{21} & \sum_{k=1}^N g_{2k} & \cdots & -g_{2N} \\ \vdots & \vdots & \ddots & \vdots \\ -g_{N1} & -g_{N2} & \cdots & \sum_{k=1}^N g_{Nk} \end{bmatrix}, \quad C = \begin{bmatrix} \sum_{k=1}^N c_{1k} & -c_{12} & \cdots & -c_{1N} \\ -c_{21} & \sum_{k=1}^N c_{2k} & \cdots & -c_{2N} \\ \vdots & \vdots & \ddots & \vdots \\ -c_{N1} & -c_{N2} & \cdots & \sum_{k=1}^N c_{Nk} \end{bmatrix}$$

$$L = \begin{bmatrix} l_{11} & l_{12} & \cdots & l_{1N} \\ l_{21} & l_{22} & \cdots & l_{2N} \\ \vdots & \vdots & \ddots & \vdots \\ l_{N1} & l_{N2} & \cdots & l_{NN} \end{bmatrix}$$

and

$$\mathbf{V} = \begin{bmatrix} V_1 \\ V_2 \\ \vdots \\ V_N \end{bmatrix}, \mathbf{I} = \begin{bmatrix} I_1 \\ I_2 \\ \vdots \\ I_N \end{bmatrix},$$

References

- [1] F. Wiesinger, P. Boesiger, and K. P. Pruessmann, “Electrodynamics and ultimate SNR in parallel MR imaging.” *Magnetic resonance in medicine : official journal of the Society of Magnetic Resonance in Medicine / Society of Magnetic Resonance in Medicine*, vol. 52, no. 2, pp. 376–90, Aug. 2004.
- [2] “The Yee Cell.” [Online]. Available: <http://fdtd.wikispaces.com/The+Yee+Cell>
- [3] R. Lattanzi, D. K. Sodickson, A. K. Grant, and Y. Zhu, “Electrodynamic constraints on homogeneity and radiofrequency power deposition in multiple coil excitations.” *Magnetic resonance in medicine : official journal of the Society of Magnetic Resonance in Medicine / Society of Magnetic Resonance in Medicine*, vol. 61, no. 2, pp. 315–34, Feb. 2009.
- [4] *Static and dynamic RF-shimming in the framework of transmit SENSE*. Proc. Int. Soc. Magn. Reson. Med., 2005.
- [5] D. O. Brunner, N. De Zanche, J. Frohlich, J. Paska, and K. P. Pruessmann, “Travelling-wave nuclear magnetic resonance,” *Nature*, vol. 457, no. 7232, pp. 994–998, Feb. 2009.
- [6] S. B. King, “RF Coil and Array Design, Construction, and Measurement for MRI Systems,” in *IEEE Int. Microw. Symp.*, Montreal, QC, Canada, 2012.
- [7] J. T. Vaughan, G. Adriany, C. J. Snyder, J. Tian, T. Thiel, L. Bolinger, H. Liu, L. DelaBarre, and K. Ugurbil, “Efficient high-frequency body coil for high-field MRI,” *Magnetic Resonance in Medicine*, vol. 52, no. 4, pp. 851–859, 2004.
- [8] T. S. Ibrahim, “A Perspective into Ultra High Field MRI RF Coils,” in *Ultra High Field Magnetic Resonance Imaging*. Boston, MA: Springer US, 2006, ch. 7, pp. 163–208.
- [9] W. L. Stutzman, *Antenna theory and design*, 1998.
- [10] P. R. P. Hoole, *Smart antennas and signal processing for communications, biomedical, and radar systems*, 2001.

- [11] D. G. Nishimura, *Principles of magnetic resonance imaging*. Stanford University, 1996.
- [12] J. Pauly, D. Nishimura, and A. Macovski, “A k-space analysis of small-tip-angle excitation. 1989.” *Journal of magnetic resonance (San Diego, Calif. : 1997)*, vol. 213, no. 2, pp. 544–57, Dec. 2011.
- [13] U. Katscher and P. Börnert, “Parallel RF transmission in MRI,” *NMR in Biomedicine*, vol. 19, no. 3, pp. 393–400, 2006.
- [14] S. Saekho, F. E. Boada, D. C. Noll, and V. A. Stenger, “Small tip angle three-dimensional tailored radiofrequency slab-select pulse for reduced B1 inhomogeneity at 3 T.” *Magnetic resonance in medicine : official journal of the Society of Magnetic Resonance in Medicine / Society of Magnetic Resonance in Medicine*, vol. 53, no. 2, pp. 479–84, Feb. 2005.
- [15] K. P. Pruessmann, M. Weiger, M. B. Scheidegger, and P. Boesiger, “SENSE: sensitivity encoding for fast MRI.” *Magnetic resonance in medicine : official journal of the Society of Magnetic Resonance in Medicine / Society of Magnetic Resonance in Medicine*, vol. 42, no. 5, pp. 952–62, Nov. 1999.
- [16] R. V. Purcell, E. M. and Torrey, H. C. and Pound, “Resonance Absorption by Nuclear Magnetic Moments in a Solid,” *Phys. Rev.*, vol. 69, no. 1-2, pp. 37—38, 1946.
- [17] J. T. Vaughan and J. R. Griffiths, *RF Coils for MRI*, ser. EMR Books. Wiley, 2012.
- [18] F. Schmitt, A. Potthast, B. Stoeckel, C. Triantafyllou, C. J. Wiggins, G. Wiggins, and L. L. Wald, “Aspects of Clinical Imaging at 7 T,” in *Ultra High Field Magnetic Resonance Imaging*, ser. Biological Magnetic Resonance. Boston, MA: Springer US, 2006, vol. 26, ch. 4, pp. 59–103.
- [19] N. Benahmed, M. Feham, and M. Khelif, “Analysis and design of a coupled coaxial line TEM resonator for magnetic resonance imaging,” *Physics in Medicine and Biology*, vol. 51, no. 8, p. 2093, Apr. 2006.
- [20] G. Bogdanov and R. Ludwig, “Coupled microstrip line transverse electromagnetic resonator model for high-field magnetic resonance imaging,” *Magnetic Resonance in Medicine*, vol. 47, no. 3, pp. 579–593, 2002.

- [21] D. B. Davidson, *Computational Electromagnetics For RF and Microwave Engineering*. Cambridge University Press, 2005.
- [22] A. Taflove, *Computational electrodynamics : the finite-difference time-domain method*. Boston: Artech House, 1995.
- [23] C. R. Paul, *Analysis of Multiconductor Transmission Lines*. Wiley, 1994.